

IHEP 94-77  
 hep-ph/9407393  
 July 1994

**FOUR WEAK GAUGE BOSON PRODUCTION  
 AT PHOTON LINEAR COLLIDER  
 AND HEAVY HIGGS SIGNAL**

G. Jikia

*Institute for High Energy Physics  
 142284, Protvino, Moscow region, Russia*

**Abstract**

We study the signals and backgrounds for a heavy Higgs boson in the processes  $\gamma\gamma \rightarrow WWW$ ,  $\gamma\gamma \rightarrow WWZ$  at the photon linear collider. The results are based on the complete tree level SM calculation for these reactions. We show that the invariant mass spectrum of central  $WW$ ,  $ZZ$  pairs is sensitive to the signal from Higgs boson with a mass up to 1 TeV at a 2 TeV linear collider for integrated luminosity of  $300 \text{ fb}^{-1}$ . At 1.5 TeV PLC Higgs boson with a mass up to 700 GeV can be studied. The nonresonant longitudinal gauge boson scattering ( $m_H = \infty$ ) can be detected in photon-photon collisions at  $e^+e^-$  center-of-mass energy of 3 TeV.

## 1. Introduction

One of the most challenging puzzles of contemporary particle physics is whether Nature indeed makes use of the Higgs mechanism of spontaneous electroweak symmetry breaking. If Higgs boson will be found below 800 GeV or so, this will be a proof of the so called weak scenario of the symmetry breaking (SB). Otherwise the scenario of the strongly interacting electroweak SB (EWSB) will take place (for recent reviews see, *e.g.*, [1]). The study of strong EWSB is one of the major motivations to built the next generation of colliders. While the potential of hadronic colliders (see, *e.g.*, [2] and references therein) as well as linear  $e^+e^-$  colliders [1, 3, 4] to explore EWSB was extensively studied, much less was done for  $\gamma\gamma$  colliders [5–8], which would provide additional unique capabilities [9, 10].

The would be “gold-plated” channel for Higgs boson production at a Photon Linear Collider (PLC)

$$\gamma\gamma \rightarrow H \rightarrow ZZ \rightarrow (q\bar{q})(l^+l^-) \quad (1.1)$$

was shown recently to be suffered from very large background from continuum  $ZZ$  pair production through  $W$  boson loop for the Higgs mass above 350 GeV [11]. So this reaction, although very promising for the measurement of the two-photon Higgs width

for  $M_H \leq 300 - 400$  GeV, provides very poor possibilities for studying of a heavy Higgs and EWSB [12, 13], unless there are strong tensor resonances within the energy reach of PLC [13].

Another very interesting potential application of photon-photon collisions at a high energy linear collider proposed recently [14, 15] is  $WW$  scattering, as illustrated in Fig. 1. In this process each photon is resolved as a  $WW$  pair. The interacting vector bosons can then scatter pair-wise or annihilate; *e.g.*, they can annihilate into a Higgs boson decaying into a  $WW$  or  $ZZ$  pair. In principle, one can use these processes

$$\begin{aligned}\gamma(1) + \gamma(2) &\rightarrow W^+(3) + W^+(4) + W^-(5) + W^-(6), \\ \gamma(1) + \gamma(2) &\rightarrow W^+(3) + W^-(4) + Z(5) + Z(6)\end{aligned}\quad (1.2)$$

for studying EWSB. In fact, this reaction at photon-photon collider is an analog of the reaction  $e^+e^- \rightarrow \nu\bar{\nu}WW(\nu\bar{\nu}ZZ)$  at linear  $e^+e^-$  collider. Event rates for the reaction (2) were estimated using effective  $W$  approximation (EWA) [16] for several models of EWSB and quite optimistic conclusions were given. However, EWA has a limited accuracy at energies of 1–2 TeV and, moreover, it does not permit to calculate the effects of the tag and veto cuts used to isolate the Higgs signal. In fact, much more diagrams (see Fig. 2) contribute to reactions (2) and it is unclear *a priori* that the background from  $WWWW$ ,  $WWZZ$  final states, all vector bosons being transverse, is manageable. We have presented our first results of the exact standard model (SM) tree level calculation for the reactions (2) in [17] and demonstrated that the observation of the heavy Higgs signal above the background is possible. Subsequently, the background was recalculated and, in addition, various models of EWSB were considered in [18] confirming calculation [17].

This paper extends our earlier results [17] on the heavy Higgs signal and background based on complete leading order calculation for reactions (2). In Section 2 we compare effective  $W_LW_L$  luminosity in photon-photon and  $e^+e^-$  collisions. The details of the calculation are given in Section 3. In Section 4 we present total cross sections for different polarizations of  $WWWW$ ,  $WWZZ$  final states. In Section 5 we will concentrate on the heavy ( $m_H = 1$  TeV) SM Higgs boson case as a prototype for models of strong EWSB and will show that its signal can be observed at a 2 TeV linear collider. We also show that Higgs boson with a mass up to 700 GeV should be relatively easily observed in photon-photon collisions at a 1.5 TeV linear collider. We conclude with some brief remarks in Section 6.

## 2. Effective $W_LW_L$ luminosity in photon-photon collisions

In this section we try to estimate the  $W_L$  flux in photon-photon collisions in comparison to that in  $e^+e^-$  collisions before calculating  $\gamma\gamma \rightarrow WWZZ$ ,  $WWWW$  cross sections. An

expression for the longitudinal  $W$  content inside the photon has been derived [19]

$$f_{W_L/\gamma}(z) = \frac{\alpha}{\pi} \left[ \frac{1-z}{z} + \frac{z(1-z)}{2} \left( \log \frac{s(1-z)^2}{M_W^2} - 2 \right) \right]. \quad (2.1)$$

The conclusion was made that the photon had a more abundant distribution function at large  $z$  than electron [20]

$$f_{W_L/e}(z) = \frac{\alpha}{4\pi \sin^2 \theta_W} \frac{1-z}{z} \quad (2.2)$$

due to the hard component with the logarithmic enhancement factor. The derivation of polarized distribution functions of quasi-real equivalent  $W_L$  inside the photon is quite a subtle problem (see, *e.g.*, discussion in [15]), so we will not rely on expressions like (1) and (2) here. We just define the effective  $W_L W_L$  luminosity in photon-photon collisions as

$$\sigma(\gamma\gamma \rightarrow W^+ W^- H) \equiv 16\pi^2 \frac{\Gamma(H \rightarrow W^+ W^-)}{m_H^3} \left. \tau \frac{d\mathcal{L}}{d\tau} \right|_{W_L W_L/\gamma\gamma}. \quad (2.3)$$

Here left hand side is the exact tree-level cross section for  $W^+ W^- H$  production in photon-photon collisions,  $\tau = m_H^2/s = M_{W_L W_L}^2/s$ . It is assumed that Higgs boson mass is large enough, so that transverse  $W_T W_T$  contribution is negligible. The form of the right hand side is derived from the expression of the cross section of Higgs boson production in  $WW$  fusion in terms of longitudinal  $W$  distribution function calculated relying on equivalent  $W_L$  approximation

$$\sigma_{EWA}(H) = 16\pi^2 \frac{\Gamma(H \rightarrow W_L^+ W_L^-)}{m_H^3} \tau \int \frac{dz}{z} f_{W_L}(z) f_{W_L}(\frac{\tau}{z}). \quad (2.4)$$

We stress again that we will not use the EWA formulas like (1,2), but instead will use the equation (3) as a definition of  $\mathcal{L}_{W_L W_L/\gamma\gamma}$ , thereby avoiding inaccuracies associated with expression (1). We believe this approach extends the applicability of EWA method to a wide kinematical region and foresees the use of any next-to-leading improved EWA distribution functions. Similarly, we define the effective  $W_L W_L$  luminosity in  $e^+ e^-$  collisions as

$$\sigma(e^+ e^- \rightarrow \nu_e \bar{\nu}_e H) \equiv 16\pi^2 \frac{\Gamma(H \rightarrow W^+ W^-)}{m_H^3} \left. \tau \frac{d\mathcal{L}}{d\tau} \right|_{W_L W_L/e^+ e^-}. \quad (2.5)$$

Fig. 3 presents the effective  $W_L W_L$  luminosity in  $\gamma\gamma$  and  $e^+ e^-$  collisions as a function of  $\tau$  for various values of center-of-mass energies. The  $W_L W_L$  luminosity in  $e^+ e^-$  collisions is almost independent of  $\sqrt{s}$  as a function of  $\tau$  at  $\tau > 0.1$  exhibiting scaling behaviour, as it is implied by (2). On the contrary, the  $W_L W_L$  luminosity in  $\gamma\gamma$  collisions does depend on photon-photon center-of-mass energy, that again can be expected from EWA distribution function (1). While at  $\sqrt{s} = 1$  TeV the  $W_L W_L$  luminosity in photon-photon collisions coincides with the luminosity in  $e^+ e^-$  collisions at large values of  $\tau$  and is slightly smaller at low values of  $\tau$ , at higher energies  $\mathcal{L}_{W_L W_L/\gamma\gamma}$  is several times larger than  $\mathcal{L}_{W_L W_L/e^+ e^-}$ . This confirms previous hopes that at multi-TeV energies photon beams can be more

efficient source of energetic  $W_L$ 's than electron beams. In fact, the larger luminosity in photon-photon collisions results from harder distribution function (1) and an additional factor of two, because both photons can produce  $W_L^+$  as well as  $W_L^-$ . However, to compare the potential of photon-photon option of linear collider with that of original  $e^+e^-$  option, one has to take into account that laser induced photon beams are not monochromatic [5]: photon spectrum depends on the product of the helicity of the electron and laser photon and the highest photon energy is bounded by

$$\omega_{max} = \frac{x_0}{x_0 + 1} E_{beam}, \quad (2.6)$$

where  $x_0$  is the machine parameter related to the electron beam energy and laser photon energy [5]

$$x_0 = \frac{4E_{beam}\omega_0}{m_e^2}. \quad (2.7)$$

The optimal value of  $x_0$  is 4.8 [5], so that the maximum photon energy fraction is  $z_{max} = 0.8$ . A more realistic effective  $W_L W_L$  luminosity in photon-photon collisions calculated taking into account the photon distribution function

$$\tau \left. \frac{d\mathcal{L}^{eff}}{d\tau}(\tau) \right|_{W_L W_L/\gamma\gamma} = \tau \int \frac{dz_1}{z_1} \frac{dz_2}{z_2} f_\gamma(z_1) f_\gamma(z_2) \left. \frac{d\mathcal{L}}{d\tau} \left( \frac{\tau}{z_1 z_2} \right) \right|_{W_L W_L/\gamma\gamma} \quad (2.8)$$

is presented in Fig. 4. We assume that the product of electron and laser helicity is  $2\lambda_e\lambda_\gamma = 2\lambda'_e\lambda'_\gamma = -0.9$ . This case gives the hardest photon spectrum for 100% polarized laser beams and 90% polarized electron beams. For initial laser beam helicities of ++ and +-, final high energy photons are produced predominantly in  $J_Z = 0$  and  $J_Z = 2$  states, respectively. The effective luminosity is about two times larger for ++ initial laser helicities, but it is more than an order of magnitude smaller than for monochromatic photons. And for all energies the  $W_L W_L$  luminosity in photon-photon collisions is now almost an order of magnitude smaller than the  $W_L W_L$  luminosity in  $e^+e^-$  collisions at the same center-of-mass energy. This fact can be easily understood. Consider, for example, the  $W_L W_L$  luminosity for 2 TeV linear collider at  $M_{W_L W_L} = 1$  TeV. The  $\mathcal{L}_{W_L W_L/\gamma\gamma}$  is two times larger than  $\mathcal{L}_{W_L W_L/e^+e^-}$  at  $\sqrt{s_{\gamma\gamma}} = \sqrt{s_{e^+e^-}} = 2$  TeV. However, the maximum photon-photon center-of-mass energy is  $z_{max}$  times smaller than  $e^+e^-$  energy. The  $W_L W_L$  luminosity in photon-photon collisions steeply rises as a function of  $\sqrt{s_{\gamma\gamma}}$  (see Fig. 5). At 1.6 TeV  $\mathcal{L}_{W_L W_L/\gamma\gamma}$  is 3 times smaller than at  $\sqrt{s_{\gamma\gamma}} = 2$  TeV. Moreover, the integral over photon-photon luminosity spectrum in the interval  $(M_{W_L W_L} + 2M_W)/\sqrt{s} = 0.6 < \sqrt{\tau} < 0.8 = z_{max}$  is 0.35. And, finally, a factor of 2 is lost because within this interval  $W_L W_L$  luminosity decreases when  $\tau$  decreases. Thus, at  $\sqrt{s} = 2$  TeV and  $M_{W_L W_L} = 1$  TeV effective  $W_L W_L$  luminosity in photon-photon collisions for realistic photon spectrum is 17 times smaller than that for monochromatic photon spectrum and 8 times smaller than  $W_L W_L$  luminosity in  $e^+e^-$  collisions.

Nevertheless, what should be emphasized, is that the luminosity of high energy photon-photon collider has a much less restrictive upper bound than that for  $e^+e^-$  collider because of different conditions at the interaction point [6–8]. And it is even stated

that such a huge luminosity as  $10^{35-36} \text{ cm}^{-2} \text{ s}^{-1}$  might be achievable in photon-photon collisions [6–8]. So, it is quite possible that the lack of  $W_L W_L$  luminosity due to non-monochromaticity of the laser induced photon spectrum can be compensated by technical advantages of the photon-photon option of the linear collider.

### 3. Matrix element

The calculation of four weak gauge boson production in photon-photon collisions involves a large number of Feynman diagrams and, so, the efficiency and numerical stability are key issues. *E.g.*, if one would calculate the square of the matrix element in unitary gauge, severe numerical cancellations would occur among the longitudinal  $p_\mu p_\nu / M_W^2$  terms, as the cross section should be non-singular in the limit  $M_W \rightarrow 0$ . At  $\sqrt{s} = 2 \text{ TeV}$  the matrix element squared of  $WWWW$ ,  $WWZZ$  production will contain the most singular terms of the order of  $(E_W/M_W)^{20} \sim 10^{16}$ , *i.e.* sixteen decimal digits will be lost! Hence, it is advantageous to use renormalizable gauge, *e.g.*, 't Hooft-Feynman gauge, and work with amplitudes directly and square them numerically. Then the most singular amplitude of four longitudinal gauge boson production will involve cancellation of terms of the order of  $(E_W/M_W)^4$ , implying a loss of accuracy of three or six digits at photon-photon center-of-mass energy of 2 TeV or 10 TeV, respectively. Further, it is possible to reduce the number of diagrams using non-linear gauges [21] where mixed photon- $W$ -Nambu-Goldstone triple vertices are absent.

There are five topologically distinctive graphs contributing to tree-level reaction with six external particles and all the diagrams describing processes (2) can be easily generated. Some Feynman diagrams are shown in Fig. 2, where also are given multiplicities of diagrams for a given topology. We used a variant of non-linear gauge which we have exploited earlier for the calculation of one-loop reaction  $\gamma\gamma \rightarrow ZZ$  [11]. In total, there are 240 diagrams for  $WWWW$  production and 104 diagrams for  $WWZZ$  production. In 't Hooft-Feynman gauge the number of diagrams is almost three times larger.

We used symbolic manipulation program FORM [22] to express the amplitude in the following form

$$\begin{aligned} \mathcal{M}(\gamma\gamma \rightarrow WWWW, WWZZ) = & \\ & \sum_{i_1 \dots i_6, j_1 \dots j_4} A_{i_1 \dots i_6, j_1 \dots j_4} (e_{i_1} e_{i_2}) (e_{i_3} p_{j_1}) (e_{i_4} p_{j_2}) (e_{i_5} p_{j_3}) (e_{i_6} p_{j_4}) \\ & + \sum_{i_1 \dots i_6, j_1, j_2} B_{i_1 \dots i_6, j_1, j_2} (e_{i_1} e_{i_2}) (e_{i_3} e_{i_4}) (e_{i_5} p_{j_1}) (e_{i_6} p_{j_2}) \\ & + \sum_{i_1 \dots i_6} C_{i_1 \dots i_6} (e_{i_1} e_{i_2}) (e_{i_3} e_{i_4}) (e_{i_5} e_{i_6}), \end{aligned} \quad (3.1)$$

here  $p_{1-6}$  and  $e_{1-6}$  are momenta and polarization vectors. This reduces the amount of numerical work when computing cross section summed over all helicity states, because coefficients  $A$ ,  $B$  and  $C$  are independent of the polarizations and they have to be computed only once. In fact, all the terms in (1) have been further bracketed in such a way, that inner brackets contain parts which are independent of  $e_{1-4}$ , and can be calculated for

given polarization vectors  $e_{5,6}$  and remain constant when summing over  $e_{1-4}$ . The next level of brackets contains parts which are independent of  $e_{1-2}$ . Actually, on a DEC Station 5000 this matrix element can be evaluated roughly 1000 times per minute. In fact, matrix element was calculated both in non-linear and 't Hooft-Feynman gauges and these two results coincided with the machine accuracy. In addition, electromagnetic gauge invariance of (1) was checked numerically  $\mathcal{M}(e_{1,2} \rightarrow p_{1,2}) = 0$ .

## 4. Cross sections

Total cross sections for  $W^+W^-ZZ$  and  $W^+W^+W^-W^-$  production in photon-photon collisions as a function of  $\gamma\gamma$  center-of-mass energy for different initial and final polarization states and two values of the Higgs boson mass  $m_H = 100$  GeV and  $m_H = \infty$  are shown in Figs. 6, 7. Different combinations like  $TTLL$  and  $TLTL$  refer to a given order of  $W^\pm$ 's and  $Z$ 's: *e.g.*,  $TLTL$  denotes  $W_T^\pm W_L^\mp Z_T Z_L$  or  $W_T^\pm W_L^\pm W_T^\mp W_L^\mp$  final states.

For the  $\gamma W^+W^-$  vertex we use Thomson limit coupling  $\alpha$ , while all the other couplings are derived from  $\alpha(M_Z)$ ,  $\sin\theta_W$  and  $\cos\theta_W$ . So, we choose  $\alpha^2\alpha(M_Z)^2$  as the overall coupling factor. Throughout this paper, we use the following set of electroweak parameters:

$$\begin{aligned} \alpha &= 1/137.036, & \alpha(M_Z) &= 1/128.82, \\ M_W &= 80.22 \text{ GeV}, & M_Z &= 91.173 \text{ GeV}, \\ \cos\theta_W &= M_W/M_Z. \end{aligned} \tag{4.1}$$

Monte-Carlo numerical integration and event generation were performed by the program package BASES/SPRING [23].

One can see that the cross sections are slightly larger for equal initial photon helicities. The dominating contribution comes from four transverse gauge boson production. The larger is the number of longitudinal gauge bosons, the smaller is the cross section. However, longitudinal gauge bosons do not decouple at large energies and all the cross sections rise with energy even for light Higgs boson. For example, for  $WWWW$  production the ratio of  $TTTT/TTTL$  is about  $(60 \div 70)\%$ . The large fraction of longitudinal polarization states production was also observed earlier for  $\gamma\gamma \rightarrow WWZ$  reaction [24]. The contributions from two longitudinal weak bosons  $TTLL$  and  $TLTL$  are about an order of magnitude smaller than that for  $TTTT$  production. The yield of  $TLLL$  and  $LLLL$  final states is even smaller, however one can see that for infinite Higgs boson mass their contribution can be orders of magnitude larger than for a 100 GeV Higgs. From Fig. 6 it is clear that large Higgs boson mass mainly affects the  $WWZZ$  cross sections with at least two longitudinal  $Z$  bosons, *e.g.*, for  $m_H = \infty$   $TTLL$  cross section increases by a factor of four at  $\sqrt{s} = 2$  TeV, while  $TLTL$  and  $LLTT$  remain almost the same. For  $WWWW$  production both  $TLTL$  and  $TTLL$  cross sections increase (see Fig. 7), but at large energy the  $TTLL$  cross section becomes dominating. This is a consequence of the well known fact that for infinitely heavy Higgs mass cross section of like charge  $W_L^\pm W_L^\pm \rightarrow W_L^\pm W_L^\pm$  scattering is larger than opposite charge  $W_L^+ W_L^- \rightarrow W_L^+ W_L^-$  scattering. Cross sections

with transverse final gauge bosons, longitudinal “spectator”  $W$  bosons,  $Z_T Z_T$ ,  $Z_L Z_T$  or  $W_T W_T W_T W_L$  final states are practically the same for  $m_H = 100$  GeV and  $m_H = \infty$ .

It is this rise of the cross section of longitudinal electro-weak gauge boson interactions that signals strong EWSB scenario [1]. This effect is illustrated in Fig. 8 where production cross sections of  $TTTT + TTTL$  as well as of final states containing at least two longitudinal gauge bosons are compared for  $m_H = 100$  GeV and  $m_H = \infty$ . As usual, we can define the heavy Higgs boson signal to be the difference between the cross section with a heavy Higgs boson and the result with a light Higgs boson, *e.g.*,

$$\sigma(\text{signal for } m_H = \infty) = \sigma(m_H = \infty) - \sigma(m_H = 100 \text{ GeV}). \quad (4.2)$$

Consequently, cross section for light Higgs boson represents the background. From Fig. 8 one can conclude that signal-to-background ratio is about 10% for total cross sections.

The relative ratios of  $WWZZ$  and  $WWWW$  cross sections can be qualitatively understood using EWA. At high energy the following relations hold for  $WW$ ,  $ZZ$  scattering cross sections integrated over  $p_\perp > p_\perp^{\min} > M_W, M_Z$  for  $m_H \sim M_W$ :

$$\sigma(W^+W^- \rightarrow W^+W^-) \simeq \sigma(W^\pm W^\pm \rightarrow W^\pm W^\pm) \simeq \frac{1}{\cos^4 \theta_W} \sigma(W^+W^- \rightarrow ZZ), \quad (4.3)$$

*i.e.*  $WW \rightarrow ZZ$  cross section is about two times smaller than the other cross sections. Therefore, the ratio of the cross sections of transverse  $WWWW$  and  $WWZZ$  production is

$$\frac{\sigma(\gamma\gamma \rightarrow WWWW)}{\sigma(\gamma\gamma \rightarrow WWZZ)} \Big|_{m_H \sim M_W} \sim \frac{\int dz_1 dz_2 f_{W/\gamma}(z_1) f_{W/\gamma}(z_2) [\sigma(W^+W^- \rightarrow W^+W^-) + \sigma(W^+W^+ \rightarrow W^+W^+)]}{\int dz_1 dz_2 f_{W/\gamma}(z_1) f_{W/\gamma}(z_2) \sigma(W^+W^- \rightarrow ZZ)} \sim 4. \quad (4.4)$$

On the other hand, ratio of the cross sections of  $WWZZ$ ,  $WWWW$  production through Higgs resonance is given by

$$\frac{\sigma(\gamma\gamma \rightarrow WWWW)}{\sigma(\gamma\gamma \rightarrow WWZZ)} \Big|_{\text{resonance}} = \frac{\Gamma(H \rightarrow W^+W^-)}{\Gamma(H \rightarrow ZZ)} \sim 2. \quad (4.5)$$

So, we conclude that signal-to-background ratio should be about two times larger for  $WWZZ$  production than for  $WWWW$  production:

$$\frac{S}{B} \Big|_{WWZZ} \sim 2 \frac{S}{B} \Big|_{WWWW}. \quad (4.6)$$

## 5. Signal of heavy Higgs boson at photon linear colider

Results presented in this section are obtained taking into account realistic photon spectrum [5]. We assume that the product of electron and laser photon helicity is  $2\lambda_e\lambda_\gamma =$

$2\lambda'_e\lambda'_\gamma = -0.9$  and  $\lambda_\gamma\lambda'_\gamma = 1$ , so that final high energy photons are produced predominantly in  $J_Z = 0$  states.

In Table 1 we summarize total cross sections for  $WWWW$ ,  $WWZZ$  production at photon-photon collider realized at 1.5, 2 and 3 TeV linear collider. Cross sections are quite large, for example more than ten thousand events of four weak boson production will take place at 2 TeV linear collider with  $\int \mathcal{L} dt = 200 \text{ fb}^{-1}$ . As expected from (5), for  $m_H = 100 \text{ GeV}$  the  $WWWW$  cross section is about four times larger than  $WWZZ$  cross section.

The scattering reaction (2) leads to two scattered  $W$ 's or  $Z$ 's emerging at large transverse momentum in the final state accompanied by two “spectator”  $W$ 's at low  $p_\perp$  focussed along the beam direction. We assume that hadronic decay modes of the central pair will be observed, *i.e.* we will not distinguish  $W$ 's from  $Z$ 's. The heavy Higgs signal can be observed in the invariant mass spectrum of the two hard scattered weak bosons. To select these  $W$ 's or  $Z$ 's we label all the final gauge bosons according to their pseudo-rapidities  $\eta_i$ :

$$|\eta_1| \geq |\eta_2| \geq |\eta_3| \geq |\eta_4|. \quad (5.1)$$

We are interested in the mass spectrum of the “central” pair  $m(V_3V_4)$ , where  $V$  denotes  $W$  or  $Z$ . The important point to note is that in the framework of EWA the initial  $W_L$ 's participating in the  $W_LW_L$  scattering have a  $1/(p_\perp^2 + M_W^2)^2$  distribution with respect to incoming photons from which they are produced. This is to be contrasted with a  $p_\perp^2/(p_\perp^2 + M_W^2)^2$  distribution of the initiating  $W_T$ 's, leading, *e.g.*, to  $W_TW_T$  scattering. Analogous effect is known to take place for  $W$  distribution in quark – (anti-) quark or  $e^+e^-$  collisions [1, 2]. The softer  $p_\perp$  distribution in the  $W_LW_L$  case has a useful consequence: the spectator  $W$ 's tend to emerge with smaller  $p_\perp$  and correspondingly smaller rapidity for  $W_LW_L$  scattering than those associated with the background processes of  $W_TW_T$  or  $W_TW_L$  scattering. Therefore, we will divide four final gauge bosons in two pairs of forward (backward)  $V_1V_2$  and central  $V_3V_4$  according to the ordering (1) and will impose different cuts on these pairs. We require that  $|\eta_{3,4}| < 1$  and, in addition, veto hard forward (backward)  $W$ 's  $|\eta_{1,2}| > 1.5$  to enhance the signal-to-background ratio. Although, all that we need is the invariant mass spectrum of  $M(V_3V_4)$ , to separate four gauge boson production from  $\gamma\gamma \rightarrow W^+W^-$  and  $\gamma\gamma \rightarrow W^+W^-Z$  backgrounds we will also tag forward (backward) spectators  $V_{1,2}$  in the region outside the dead cone along the beam direction  $|\eta_{1\div 4}| < \eta_0$ , where  $\eta_0$  is determined by the acceptance of experimental installation.

The experimental signature is then given by four central hard jets from  $V_3V_4$  decay with a branching ratio of 49% and jets or leptons in forward and backward regions from the decay of spectator  $W$ 's. We have not modelled  $W$ ,  $Z$  decays, so cuts will be imposed on momenta of vector bosons.  $W$ ,  $Z$  pairs can be selected using the good knowledge of the  $W$ ,  $Z$  mass. We assume that the procedure of  $W$  pair reconstruction at 500 GeV  $e^+e^-$  collider [25] can be applied. From four central jets two jet combinations are selected which have masses closest as possible to the  $W$ ,  $Z$  mass:

$$\min \left[ (M_{(1)} - M_{W,Z})^2 + (M_{(2)} - M_{W,Z})^2 \right]. \quad (5.2)$$

The masses scatter significantly: only 38% of the  $W$ ,  $Z$  pair events are in the region

$|M_{(1,2)} - M_{W,Z}| < 10$  GeV [25]. We assume that the same efficiency of central  $W, Z$  mass reconstruction is applied for our study. Reconstructing  $W, Z$  masses most of the QCD backgrounds should be rejected. Backgrounds from  $\gamma\gamma \rightarrow t\bar{t}$  can be eliminated by top-quark mass reconstruction and  $b$ -tagging [25].

For the reaction  $\gamma\gamma \rightarrow WWZZ$  it is possible to test our procedure of separation of hard scattered  $Z$ 's from spectator  $W$ 's based on (1). In Figs. 9-11 various distributions of  $W, Z$  bosons and corresponding distributions based on labeling (1) are shown at  $\sqrt{s_{e^+e^-}} = 2$  TeV and  $m_H = 1$  TeV and 100 GeV. It is assumed that either  $M(ZZ)$  or  $M(V_3V_4)$  is greater than 500 GeV. In Fig. 9 pseudo-rapidity distributions are presented for  $Z$  and  $W$  bosons as well as corresponding distributions for mean rapidity of  $V_3V_4$  and  $V_1V_2$  pair.  $Z$  bosons have central rapidity distribution peaking at  $\eta_Z = 0$ . Spectator  $W$ 's have rapidity distribution peaking in the forward-backward direction. For  $m_H = 1$  TeV the  $W$  distribution peaks at  $\eta_W \simeq \pm 1.5$ , while for 100 GeV Higgs the background peaks at  $\eta_W \simeq \pm 1$ . The  $\langle\eta_{3,4}\rangle$  and  $\langle\eta_{1,2}\rangle$  distributions roughly follow  $\eta_Z$  and  $\eta_W$  distributions, respectively. Fig. 10 presents  $p_\perp$  distributions.  $p_\perp^W$  and  $p_\perp^{1,2}$  distributions are peaking at small values of  $p_\perp < 100$  GeV, while  $p_\perp^Z$  and  $p_\perp^{3,4}$  distributions are wide and peak at  $p_\perp \sim 250$  GeV. The 1 TeV Higgs signal enriches large- (low-)  $p_\perp$  tail of the  $p_\perp^Z$  ( $p_\perp^W$ ) distributions. From Fig. 11 one can see that the transverse momentum distributions of  $ZZ$  and  $V_3V_4$  pair are again quite similar. Unlike the  $p_\perp^Z$  ( $p_\perp^{3,4}$ ) distributions, most of the 1 TeV Higgs signal lies at  $p_\perp^{ZZ}, p_\perp^{3+4} < 200$  GeV. Figs. 12-13 show the pseudo-rapidity and transverse momentum distributions for the reaction  $\gamma\gamma \rightarrow WWWW$  for  $M(V_3V_4) > 500$  GeV. They look similar to corresponding distributions in Figs. 9-11.

The  $M(V_3V_4)$  invariant mass distribution for the signal ( $m_H = 1$  TeV) and background ( $m_H = 100$  GeV) are shown in Fig. 14 at  $\sqrt{s_{e^+e^-}} = 2$  TeV assuming that the annual integrated luminosity is  $300 \text{ fb}^{-1}$ . The luminosity is derived from rescaling of  $20 \text{ fb}^{-1}$  for 500 GeV NLC to keep a roughly constant event rate for  $\sigma_{\text{point}} = 4\pi\alpha^2/3s$ . The rapidity cuts  $|\eta_{1\div 4}| < 3$ ,  $|\eta_{3,4}| < 1$  and  $|\eta_{1,2}| > 1.5$  are imposed. The enhancement for  $m_H = 1$  TeV in the region  $M(V_3V_4) > 500$  GeV is clearly seen in all the histograms. As predicted from (6), the signal-to-background ratio is about two times larger for  $WWZZ$  than for  $WWWW$  reaction. Also, for  $\gamma\gamma \rightarrow WWZZ$  reaction the  $M(V_3V_4)$  invariant mass spectrum looks almost the same as  $M(ZZ)$  one.

We summarize our results for  $m_H = 1$  TeV and  $m_H = \infty$  in Table 2. This table gives the signal and background event rates as a function of the dead cone along the photon beams direction. The pseudo-rapidity cuts  $\eta_0 = 3, 2.5$  correspond to approximately  $5^\circ$  and  $10^\circ$  dead cone, respectively. Hadronic branching ratio of 49% and 38% efficiency of the  $W, Z$  pair mass reconstruction are included. From the Table 2 is apparent that a 1 TeV Higgs boson can be observable at 2 TeV PLC at  $5\sigma$  level even for large  $10^\circ$  dead cone. Comparing Tables 1 and 2 one can see that while the signal contributes only about 10% to the total cross section for  $m_H = 1$  TeV, appropriate cuts permit to enhance the signal-to-background ratio by an order of magnitude. While the signal-to-backgroud ratio is two times larger for  $WWZZ$  final state, due to a four times larger statistics reaction  $\gamma\gamma \rightarrow WWWW$  gives almost the same statistical significance of the Higgs signal. The “spectator”  $W$  veto  $\eta_{1,2} > 1.5$  enhances the  $S/B$  ratio in 2-3 times, but at the expense of

large loss in statistics, so that statistical significance is almost the same with or without the forward  $W$  veto. It is important to have as good as possible coverage in forward-backward directions. Changing  $\eta_0$  from 3 to 2.5 we diminish the signal in 1.5-2 times. As for infinitely heavy Higgs boson, the statistical significance of the signal is always below  $3\sigma$  for any realistic detector acceptance.

Fig. 15 and Table 3 show the signal and background for  $m_H = 500$  GeV and  $m_H = 700$  GeV at  $\sqrt{s_{e^+e^-}} = 1.5$  TeV assuming the annual integrated luminosity of  $200 \text{ fb}^{-1}$ . The pronounced peak from 500 GeV Higgs boson should be easily observable with statistical significance greater than  $10\sigma$ . For  $m_H = 700$  GeV the peak is already quite wide, but still it should be observable at the level of about  $4\sigma$ . So, in principle, the reactions of  $WWWW, WWZZ$  production in photon-photon collisions allow to observe Higgs boson heavier than 400 GeV, which is the maximum Higgs mass detectable in the reaction  $\gamma\gamma \rightarrow ZZ$  [11]. However, for the former case Higgs boson production emerges from the  $W$  fusion reaction and has nothing to do with two-photon Higgs width, which can be measured for lighter Higgs in  $\gamma\gamma \rightarrow ZZ$  reaction. It is hardly possible to push the observable Higgs mass well above 700 GeV at 1.5 TeV machine.

Finally, to exemplify PLC potential to probe nonresonant strong  $W_LW_L, Z_LZ_L$  scattering in Fig. 16 and Table 4 we show results for infinitely heavy Higgs boson at  $\sqrt{s_{e^+e^-}} = 3$  TeV assuming the annual integrated luminosity of  $300 \text{ fb}^{-1}$ . To avoid problems with non-unitarity of cross section of the longitudinal gauge boson scattering at high energy we assumed that  $M(V_3V_4) < 1.5$  TeV. The excess of events for  $m_H = \infty$  should be observable at  $4\sigma$  level even for the worst detector coverage.

## 6. Conclusions

We have demonstrated that significant signal from 1 TeV Higgs resonance can be observed in the hadronic final states in photon-photon collisions at 2 TeV linear collider for integrated luminosity of  $300 \text{ fb}^{-1}$ . The nonresonant strong scattering of longitudinal weak gauge bosons can be studied at larger collision energy of 3 TeV. Higgs mass range up to 700 GeV can be covered at 1.5 TeV PLC for integrated luminosity of  $200 \text{ fb}^{-1}$ .

The most important question is, certainly, comparison of the potential of photon-photon collider with that of other machines. For hadronic and  $e^+e^-$  colliders much more detailed investigations were done including decays of final  $W$ 's and  $Z$ 's and detector simulations [1, 2, 4]. For example, conclusion is done [4] that the signal from 1 TeV Higgs boson is distinguishable from the case of massless Higgs at the center-of-mass energy of  $e^+e^-$  collider of 1.5 TeV and integrated luminosity of  $200 \text{ fb}^{-1}$ . However, it is also found that the integrated luminosity of  $310 \text{ fb}^{-1}$  and  $80 \text{ fb}^{-1}$  is needed to discriminate the  $m_H = \infty$  signal at  $3\sigma$  level at 2 TeV and 3 TeV linear collider, respectively. So, we can very roughly estimate that potential of 2 TeV linear collider in photon-photon mode is at least the same as that of 1.5 TeV  $e^+e^-$  collider, provided that their luminosities are the same. The optimistic conclusion of [18] that luminosity of  $10 \text{ fb}^{-1}$  could suffice to study strong EWSB in photon-photon collisions at 2.5 TeV  $e^+e^-$  collider is applicable only to resonant models of the SB, *e.g.* SM Higgs boson with a mass of 1 TeV. To observe

non-resonant strong  $W_L$ ,  $Z_L$  scattering ( $m_H = \infty$ ) in  $\gamma\gamma$  collisions, which is an adequate goal at  $e^+e^-$  energy above 2 TeV, definitely the luminosity above  $100 \text{ fb}^{-1}$  is needed. In addition, we should mention that conclusions of [1, 3, 4] are based on the assumption that the background from  $e^+e^- \rightarrow e^\pm\nu W^\mp Z$ , which is comparable to the signal, can be suppressed by distinguishing the  $W$ 's from  $Z$ 's in the final state. But the accuracy of calorimetric measurement of the di-jet invariant mass is as large as the intrinsic  $W-Z$  mass difference and it is not clear that high  $W-Z$  separation efficiency can be achieved.

Finally, we would like to point out that if due to specific conditions at the interaction point a huge luminosity  $10^{35-36} \text{ cm}^{-2} \text{ s}^{-1}$  is technically achievable in high energy photon-photon collisions [6-8] and if it will be possible to make experiments at such a luminosity, photon-photon option will become very competitive with normal  $e^+e^-$  mode of linear collider.

## Acknowledgements

I am grateful to M. Berger, E. Boos, F. Boudjema, S. Brodsky, M. Chanowitz, K. Cheung, I. Ginzburg, T. Han, V. Ilyin, F. Richard, V. Serbo and V. Telnov for many helpful discussions. This work was supported, in part, by the INTAS-93-1180 grant.

## References

- [1] M.S. Chanowitz, in Proc. of the *2-nd KEK Topical Conference on  $e^+e^-$  Collision Physics*, Tsukuba, Japan, November 26-29, 1991;  
 K.-I. Hikasa, in *Physics and Experiments with Linear  $e^+e^-$  Colliders*, Saariselkä, Finland, 1992, Ed. R. Orava *et al.*, World Scientific, p. 451;  
 T. Han, in *Physics and Experiments with Linear  $e^+e^-$  Colliders*, Waikoloa, Hawaii, 1993, Ed. F.A. Harris *et al.*, World Scientific, vol. I, p. 270.
- [2] J. Bagger, V. Barger, K. Cheung, J. Gunion, T. Han, G.A. Ladinsky, R. Rosenfeld, and C.P. Yuan, *Phys. Rev.* **D49** (1994) 1246.
- [3] K. Hagiwara, J. Kanzaki, and H. Murayama, KEK Report No. 91-4 (March 1991).
- [4] Y. Kurihara, R. Najima, *Phys. Lett.* **B301** (1993) 292;  
 Y. Kurihara, R. Najima, KEK-Preprint-93-90, August 1993.
- [5] I.F. Ginzburg, G.L. Kotkin, V.G. Serbo and V.I. Telnov, *Pis'ma ZhETF* **34** (1981) 514; *Nucl. Instr. and Methods* **205** (1983) 47;  
 I.F. Ginzburg, G.L. Kotkin, S.L. Panfil, V.G. Serbo and V.I. Telnov, *Nucl. Instr. and Methods* **219** (1984) 5.
- [6] V.I. Telnov, *Nucl. Instr. and Methods* **A294** (1990) 72.

- [7] V.I. Telnov, Proceedings of *Workshop on Physics and Experiments with Linear  $e^+e^-$  Colliders*, Waikoloa, Hawaii, 1993, Ed. F.A. Harris *et al.*, World Scientific, vol. II, p. 551; Proceedings of *Workshop on gamma-gamma colliders*, March 28-31, 1994, Lawrence Berkeley Laboratory, *Nucl. Instr. and Methods A*, to be published.
- [8] V.E. Balakin, Proceedings of *Workshop on gamma-gamma colliders*, March 28-31, 1994, Lawrence Berkeley Laboratory, *Nucl. Instr. and Methods A*, to be published.
- [9] S.J. Brodsky, *ibid.*
- [10] M.S. Chanowitz, *ibid.*
- [11] G.V. Jikia, *Phys. Lett.* **298B** (1993) 224, *Nucl. Phys.* **B405** (1993) 24; B. Bajc, *Phys. Rev.* **D48** (1993) 1907; M.S. Berger, *Phys. Rev.* **D48** (1993) 5121; D.A. Dicus, C. Kao, *Phys. Rev.* **D49** (1994) 1265; H. Veltman, report SACLAY-SPHT-93-111, October 1993.
- [12] R. Rosenfeld, *Mod. Phys. Lett.* **A9** (1994) 735.
- [13] M.S. Berger, M.S. Chanowitz, LBL-35746, hep-ph/9406413, Proceedings of *Workshop on gamma-gamma colliders*, March 28-31, 1994, Lawrence Berkeley Laboratory, *Nucl. Instr. and Methods A*, to be published.
- [14] S.J. Brodsky, in *Physics and Experiments with Linear  $e^+e^-$  Colliders*, Waikoloa, Hawaii, 1993, Ed. F.A. Harris *et al.*, World Scientific, vol. I, p. 295.
- [15] F. Boudjema, Convener's talk (*W* Working group), 1st meeting of the Workshop on  *$e^+e^-$  Collisions at 500 GeV: the Physics Potential*, Munich-Annecy-Hamburg, Munich, Nov. 1992; M. Baillargeon, G. Belanger, and F. Boudjema, ENSLAPP-A-473-94, May 1994.
- [16] K. Cheung, *Phys. Lett.* **B323** (1994) 85, Proceedings of *Workshop on gamma-gamma colliders*, March 28-31, 1994, Lawrence Berkeley Laboratory, *Nucl. Instr. and Methods A*, to be published
- [17] G. Jikia, Proceedings of *Workshop on gamma-gamma colliders*, March 28-31, 1994, Lawrence Berkeley Laboratory, *Nucl. Instr. and Methods A*, to be published and hep-ph/9406595.
- [18] K. Cheung, NUHEP-TH-94-13, June 1994, hep-ph/9406228.
- [19] K. Hagiwara, I. Watanabe and P.M. Zerwas, *Phys. Lett.* **B278** (1992) 187.
- [20] S. Dawson, *Nucl. Phys.* **B249** (1984) 42; G.L. Kane, W.W. Repko and W.B. Rolnick, *Phys. Lett.* **B148** (1984) 367.

- [21] K. Fujikawa, *Phys. Rev.* **D7** (1973) 393;  
 M. Base and N.D. Hari Dass, *Ann. Phys.* **94** (1975) 349;  
 M.B. Gavela, G. Girardi, C. Malleville and P. Sorba, *Nucl. Phys.* **B193** (1981) 257;  
 N.G. Deshpande and M. Nazerimonfared, *Nucl. Phys.* **B213** (1983) 390;  
 F. Boudjema, *Phys. Lett.* **B187** (1987) 362.
- [22] J.A.M. Vermaasen, Symbolic Manipulation with FORM, published by CAN, Kruislaan 413, 1098 SJ Amsterdam, 1991, ISBN 90-74116-01-9.
- [23] S. Kawabata, *Comp. Phys. Comm.* **41** (1986) 127;  
 T. Ishikawa, T. Kaneko, K. Kato, S. Kawabata, Y. Shimizu and H. Tanaka, KEK Report 92-19, February 1993.
- [24] M. Baillargeon, F. Boudjema, *Phys. Lett.* **B317** (1993) 371.
- [25] M. Frank, P. Mättig, R. Settles, W. Zeuner, Proceedings of the Workshop on  $e^+e^-$  collisions at 500 GeV: the physics potential, Ed. P.M. Zerwas, DESY 92-123A, Part A, p. 223.

## Figure captions

Fig. 1.  $WW$  scattering at a photon-photon collider.

Fig. 2. Typical Feynman diagrams corresponding to five different topologies contributing to the reactions  $\gamma\gamma \rightarrow WWWW$ ,  $WWZZ$ . The numbers below the diagram denote the total number of graphs belonging to a given topology. The numbers in parentheses refer to the reaction  $\gamma\gamma \rightarrow WWZZ$

Fig. 3. The  $W_LW_L$  luminosity in photon-photon and  $e^+e^-$  collisions as a function of  $\tau = M_{W_LW_L}^2/s$  at the center-of-mass energy of 1, 2, 3, 5 and 10 TeV. For  $e^+e^-$  case upper curves correspond to lower energy, while for photon-photon case, on the contrary, upper curves correspond to larger energy.

Fig. 4. The  $W_LW_L$  luminosity in photon-photon collisions, calculated taking into account realistic photon spectrum, and in  $e^+e^-$  collisions as a function of  $M_{W_LW_L}$  at the center-of-mass energy of 1, 2, 3, 5 and 10 TeV. Upper curves correspond to larger energy.  $++$  and  $+-$  refer to initial laser photon helicities  $\lambda_\gamma\lambda'_\gamma = +1$  and  $-1$ , respectively.

Fig. 5. The  $W_LW_L$  luminosity in photon-photon collisions as a function of  $\sqrt{s_{\gamma\gamma}}$  for  $M_{W_LW_L} = 0.5, 1$  and  $1.5$  TeV.

Fig. 6. Cross sections for different polarization states of initial and final particles of the reaction  $\gamma\gamma \rightarrow W^+W^-ZZ$  for  $m_H = 100$  GeV and  $m_H = \infty$  as a function of  $\gamma\gamma$  center-of-mass energy.  $++$  and  $+-$  refer to initial photon helicities. Solid line denotes total cross section. Also are shown curves for different polarization states of  $W^+W^-ZZ$ :  $TTTT$  (.....);  $TTTL$  (- - - -) and  $TLTT$  (— · — · —);  $TLTL$  (— - -),  $TTLL$  (— - -) and  $LLTT$  (— — —);  $TLLL$  (· · · ·) and  $LLLT$  (· · · ·);  $LLLL$  (· - - -).

Fig. 7. Cross sections for different polarization states of initial and final particles of the reaction  $\gamma\gamma \rightarrow W^+W^+W^-W^-$  for  $m_H = 100$  GeV and  $m_H = \infty$  as a function of  $\gamma\gamma$  center-of-mass energy.

Fig. 8. Comparison between the cross sections for  $m_H = 100$  GeV and  $m_H = \infty$  for equal and opposite helicities of the initial photons. For the reaction  $\gamma\gamma \rightarrow WWWW$  the following cross sections are shown: total cross section (solid line); the  $TTTT + TTTL$  cross section (dotted line); the sum of cross sections with at least two longitudinal final  $W$ 's (dashed line). For the reaction  $\gamma\gamma \rightarrow WWZZ$  corresponding cross sections are denoted by solid, dotted and dash-dotted lines.

Fig. 9. Pseudo-rapidity distributions for the reaction  $\gamma\gamma \rightarrow WWZZ$  for  $m_H = 100$  (shaded histogram) and 1000 GeV at  $\sqrt{s_{e^+e^-}} = 2$  TeV for integrated luminosity of

300  $\text{fb}^{-1}$ .

Fig. 10.  $p_{\perp}$  distributions for the reaction  $\gamma\gamma \rightarrow WWZZ$  for  $m_H = 100$  (shaded histogram) and 1000 GeV at  $\sqrt{s_{e^+e^-}} = 2$  TeV for integrated luminosity of 300  $\text{fb}^{-1}$ .

Fig. 11.  $p_{\perp}^{ZZ}$  and  $p_{\perp}^{3+4}$  distributions for the reaction  $\gamma\gamma \rightarrow WWZZ$  for  $m_H = 100$  (shaded histogram) and 1000 GeV at  $\sqrt{s_{e^+e^-}} = 2$  TeV for integrated luminosity of 300  $\text{fb}^{-1}$ .

Fig. 12. Pseudo-rapidity distributions for the reaction  $\gamma\gamma \rightarrow WWWW$  for  $m_H = 100$  (shaded histogram) and 1000 GeV at  $\sqrt{s_{e^+e^-}} = 2$  TeV for integrated luminosity of 300  $\text{fb}^{-1}$ .

Fig. 13.  $p_{\perp}$  distributions for the reaction  $\gamma\gamma \rightarrow WWWW$  for  $m_H = 100$  (shaded histogram) and 1000 GeV at  $\sqrt{s_{e^+e^-}} = 2$  TeV for integrated luminosity of 300  $\text{fb}^{-1}$ .

Fig. 14. Invariant mass  $M(V_3V_4)$  distributions for  $WWWW$ ,  $WWZZ$  and  $WWWW + WWZZ$  production in  $\gamma\gamma$  collisions at 2 TeV linear collider for  $m_H = 100$  (shaded histogram) and 1000 GeV for integrated luminosity of 300  $\text{fb}^{-1}$ . The last histogram assumes that  $W$ 's are distinguished from  $Z$ 's for  $WWZZ$  production, the corresponding cuts are  $|\eta_{1\div 4}| < 3$ ,  $|\eta_Z| < 1$  and  $|\eta_W| > 1.5$ . No branching ratios or efficiencies are included.

Fig. 15. Invariant mass distributions for  $WWWW$ ,  $WWZZ$  and  $WWWW + WWZZ$  production in  $\gamma\gamma$  collisions at 1.5 TeV linear collider for  $m_H = 100, 500$  and  $700$  GeV for integrated luminosity of 200  $\text{fb}^{-1}$ .

Fig. 16. Invariant mass distributions for  $WWWW$ ,  $WWZZ$  and  $WWWW + WWZZ$  production in  $\gamma\gamma$  collisions at 3 TeV linear collider for  $m_H = 100$  GeV and  $\infty$  for integrated luminosity of 300  $\text{fb}^{-1}$ .

## Table captions

Table 1: Total cross sections (in fb) for  $\gamma\gamma \rightarrow W^+W^+W^-W^-$  and  $\gamma\gamma \rightarrow W^+W^-ZZ$  reactions at  $\sqrt{s_{e^+e^-}} = 1.5, 2$  and  $3$  TeV.

Table 2: Event rates for signal ( $S$ ) and background ( $B$ ), signal-to-background ratio and the number of standard deviations for  $WWWW$ ,  $WWZZ$  final states and their sum at  $\sqrt{s_{e^+e^-}} = 2$  TeV,  $m_H = 1$  TeV and  $\infty$  for various values of the dead cone angle and various cuts. The invariant mass  $M_{34}$  of central pair is required to be greater than 500 GeV. Branching ratio of 49% for hadronic decays of central  $WW$ ,  $ZZ$  pair and efficiency of central  $W$ ,  $Z$  mass reconstruction of 38% are included.

Table 3: Events rates at  $\sqrt{s_{e^+e^-}} = 1.5$  TeV and  $m_H = 500$  and  $700$  GeV. For  $m_H = 500$  GeV the invariant mass  $M_{34}$  of central pair is required to be  $400 \text{ GeV} < M_{34} < 600 \text{ GeV}$ ; for  $m_H = 700$  GeV  $500 \text{ GeV} < M_{34} < 900 \text{ GeV}$ .

Table 4: Events rates at  $\sqrt{s_{e^+e^-}} = 3$  TeV and  $m_H = \infty$ . The invariant mass  $M_{34}$  of central pair is required to be  $500 \text{ GeV} < M_{34} < 1.5 \text{ TeV}$ .

Table 1:

$\sqrt{s_{e^+e^-}} = 1.5 \text{ TeV}$	$\gamma\gamma \rightarrow WWWW$			$\gamma\gamma \rightarrow WWZZ$		
$m_H, \text{ TeV}$	0.1	0.5	0.7	0.1	0.5	0.7
$\sigma_{tot}, \text{ fb}$	30.6	40.4	34.7	6.85	11.6	8.92
$\sqrt{s_{e^+e^-}} = 2 \text{ TeV}$	$\gamma\gamma \rightarrow WWWW$			$\gamma\gamma \rightarrow WWZZ$		
$m_H, \text{ TeV}$	0.1	1	$\infty$	0.1	1	$\infty$
$\sigma_{tot}, \text{ fb}$	61.1	68.1	65.6	14.3	17.9	16.1
$\sqrt{s_{e^+e^-}} = 3 \text{ TeV}$	$\gamma\gamma \rightarrow WWWW$			$\gamma\gamma \rightarrow WWZZ$		
$m_H, \text{ TeV}$	0.1	$\infty$		0.1	$\infty$	
$\sigma_{tot}, \text{ fb}$	133	147		32.2	38.3	

Table 2:

$\sqrt{s_{e^+e^-}} = 2 \text{ TeV}; \int \mathcal{L} dt = 300 \text{ fb}^{-1}; m_H = 1 \text{ TeV}; \Gamma_H = 0.52 \text{ TeV}$								
$WWWW$	$ \eta_{1,2}  > 1.5,  \eta_{3,4}  < 1$				$ \eta_{3,4}  < 1$			
	$S$	$B$	$S/B$	$S/\sqrt{B}$	$S$	$B$	$S/B$	$S/\sqrt{B}$
—	65	78	0.83	7.3	149	453	0.33	7.0
$ \eta_{1\div 4}  < 3$	42	66	0.63	5.2	117	429	0.27	5.6
$ \eta_{1\div 4}  < 2.5$	22	50	0.44	3.1	86	389	0.22	4.3
$WWZZ$	$ \eta_{1,2}  > 1.5,  \eta_{3,4}  < 1$				$ \eta_{3,4}  < 1$			
	$S$	$B$	$S/B$	$S/\sqrt{B}$	$S$	$B$	$S/B$	$S/\sqrt{B}$
—	41	24	1.7	8.3	78	165	0.47	6.1
$ \eta_{1\div 4}  < 3$	25	20	1.3	5.7	57	157	0.36	4.6
$ \eta_{1\div 4}  < 2.5$	15	15	1.0	3.9	40	146	0.28	3.3
$WWWW$ + $WWZZ$	$ \eta_{1,2}  > 1.5,  \eta_{3,4}  < 1$				$ \eta_{3,4}  < 1$			
	$S$	$B$	$S/B$	$S/\sqrt{B}$	$S$	$B$	$S/B$	$S/\sqrt{B}$
—	105	101	1.0	10	227	617	0.37	9.1
$ \eta_{1\div 4}  < 3$	67	86	0.78	7.3	174	586	0.30	7.2
$ \eta_{1\div 4}  < 2.5$	37	65	0.57	4.6	126	535	0.24	5.4
$\sqrt{s_{e^+e^-}} = 2 \text{ TeV}; \int \mathcal{L} dt = 300 \text{ fb}^{-1}; m_H = \infty$								
$WWWW$ + $WWZZ$	$ \eta_{1,2}  > 1.5,  \eta_{3,4}  < 1$				$ \eta_{3,4}  < 1$			
	$S$	$B$	$S/B$	$S/\sqrt{B}$	$S$	$B$	$S/B$	$S/\sqrt{B}$
—	33	101	0.33	3.3	88	617	0.14	3.5
$ \eta_{1\div 4}  < 3$	21	86	0.24	2.3	67	586	0.11	2.8
$ \eta_{1\div 4}  < 2.5$	8	65	0.13	1.0	46	535	0.09	2.0

Table 3:

$\sqrt{s_{e^+e^-}} = 1.5 \text{ TeV}; \int \mathcal{L} dt = 200 \text{ fb}^{-1}; m_H = 500 \text{ GeV}; \Gamma_H = 64 \text{ GeV}$								
$WWWW$ $+ WWZZ$	$ \eta_{1,2}  > 1.5,  \eta_{3,4}  < 1$				$ \eta_{3,4}  < 1$			
	$S$	$B$	$S/B$	$S/\sqrt{B}$	$S$	$B$	$S/B$	$S/\sqrt{B}$
—	122	29	4.2	23	236	197	1.2	17
$ \eta_{1\div 4}  < 3$	85	26	3.3	17	186	189	0.98	14
$ \eta_{1\div 4}  < 2.5$	50	20	2.5	11	134	174	0.77	10

$\sqrt{s_{e^+e^-}} = 1.5 \text{ TeV}; \int \mathcal{L} dt = 200 \text{ fb}^{-1}; m_H = 700 \text{ GeV}; \Gamma_H = 180 \text{ GeV}$								
$WWWW$ $+ WWZZ$	$ \eta_{1,2}  > 1.5,  \eta_{3,4}  < 1$				$ \eta_{3,4}  < 1$			
	$S$	$B$	$S/B$	$S/\sqrt{B}$	$S$	$B$	$S/B$	$S/\sqrt{B}$
—	27	20	1.4	6.0	67	180	0.37	5.0
$ \eta_{1\div 4}  < 3$	20	18	1.2	4.9	56	174	0.32	4.3
$ \eta_{1\div 4}  < 2.5$	14	14	1.0	3.7	45	163	0.28	3.5

Table 4:

$\sqrt{s_{e^+e^-}} = 3 \text{ TeV}; \int \mathcal{L} dt = 300 \text{ fb}^{-1}; m_H = \infty$								
$WWWW$ $+ WWZZ$	$ \eta_{1,2}  > 1.5,  \eta_{3,4}  < 1$				$ \eta_{3,4}  < 1$			
	$S$	$B$	$S/B$	$S/\sqrt{B}$	$S$	$B$	$S/B$	$S/\sqrt{B}$
—	206	296	0.70	12	335	1116	0.30	10
$ \eta_{1\div 4}  < 3$	94	230	0.41	6.2	194	1002	0.19	6.1
$ \eta_{1\div 4}  < 2.5$	48	151	0.32	3.9	120	855	0.14	4.1

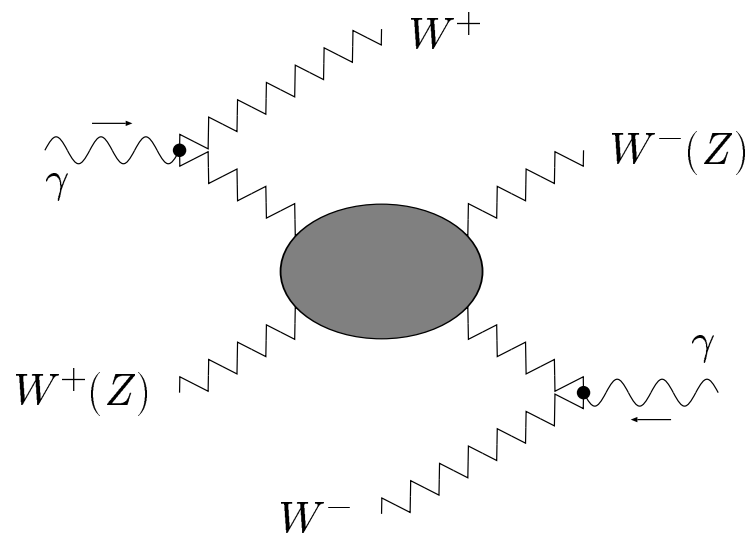


Figure 1.

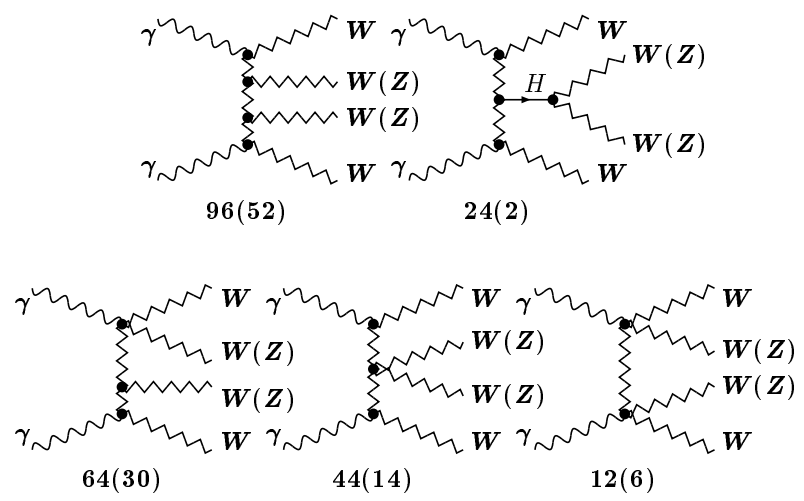


Figure 2.

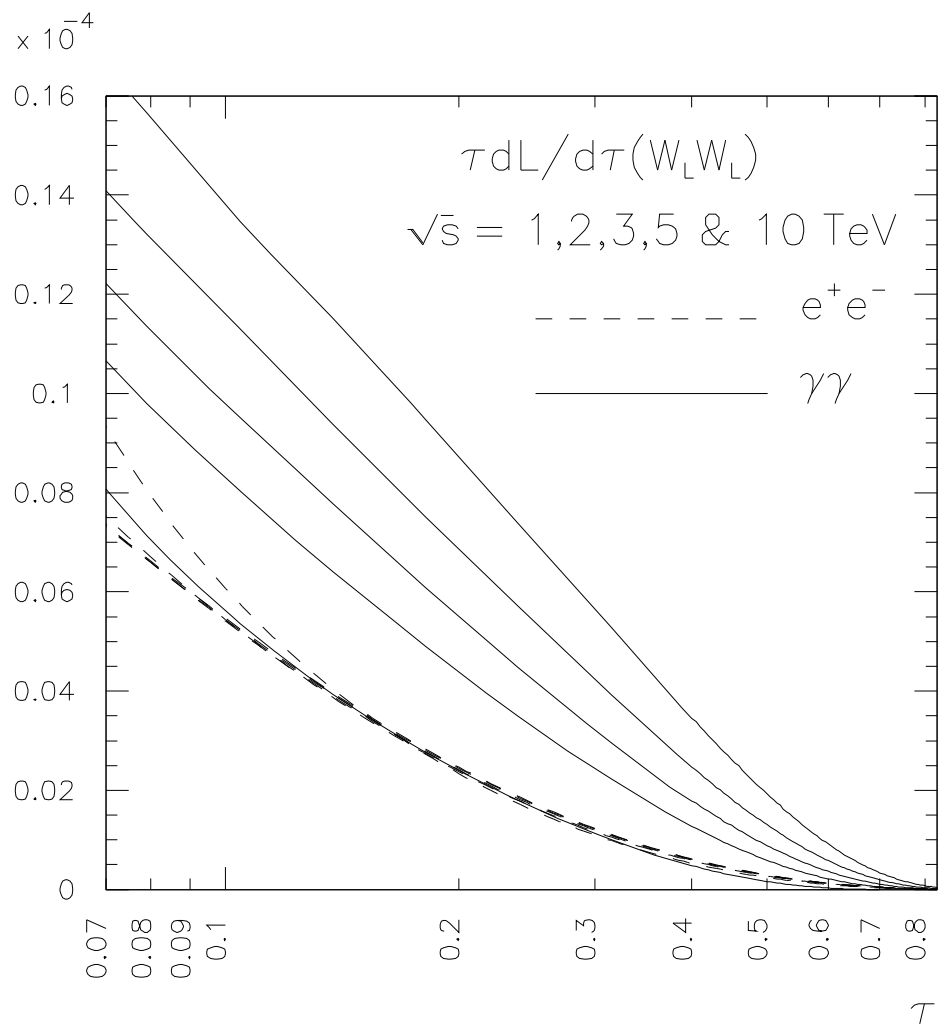


Figure 3.

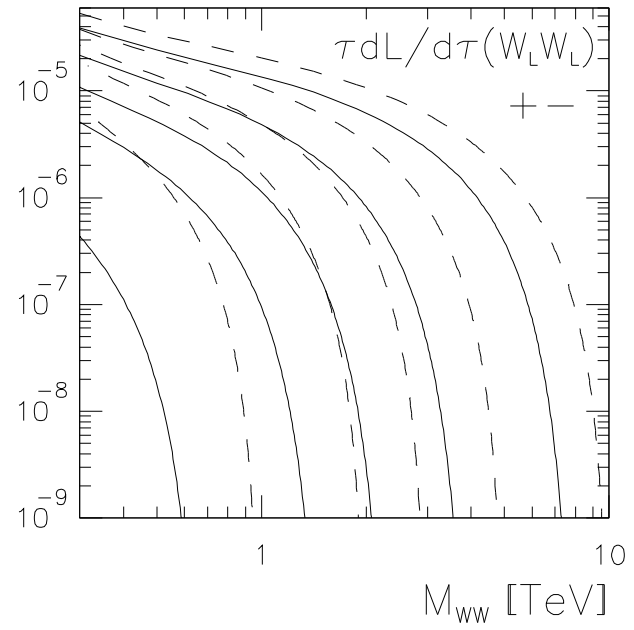
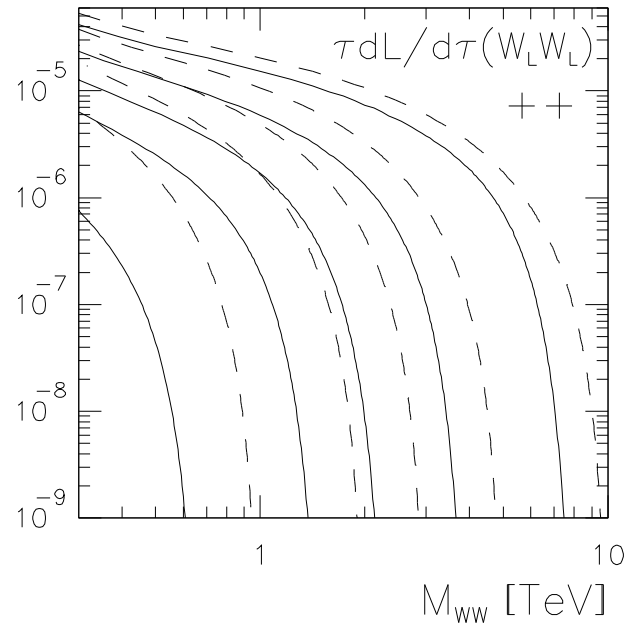


Figure 4.

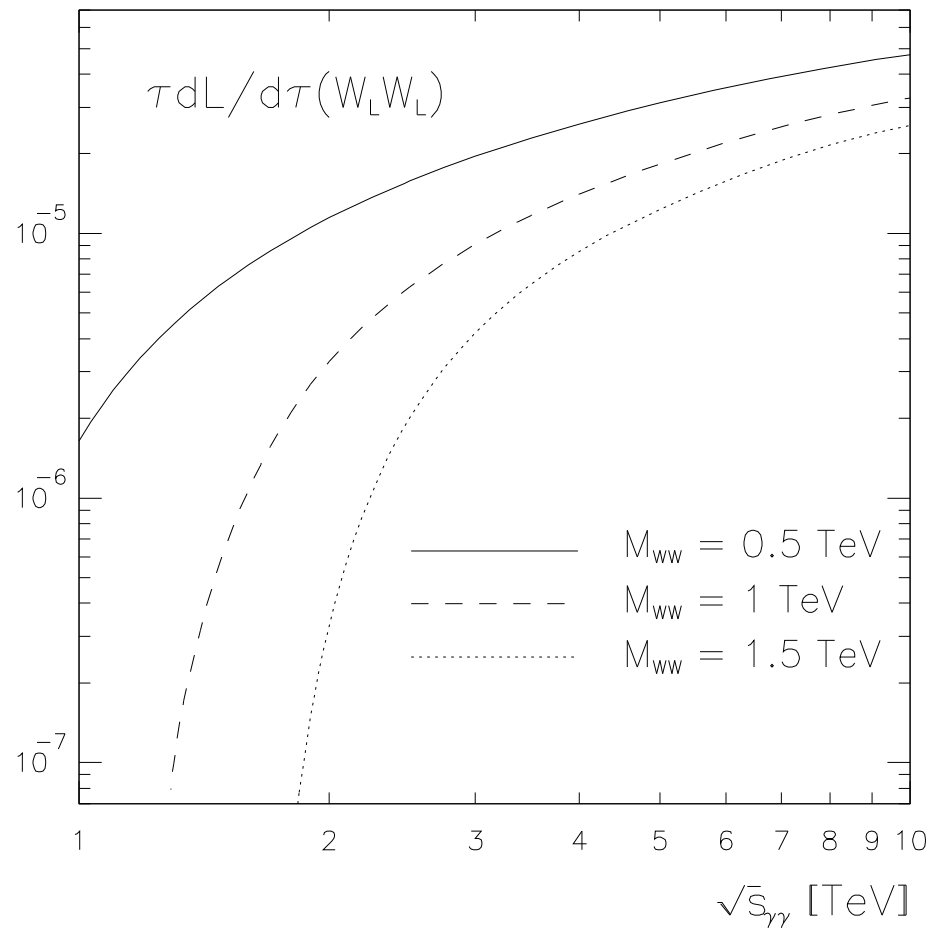


Figure 5.

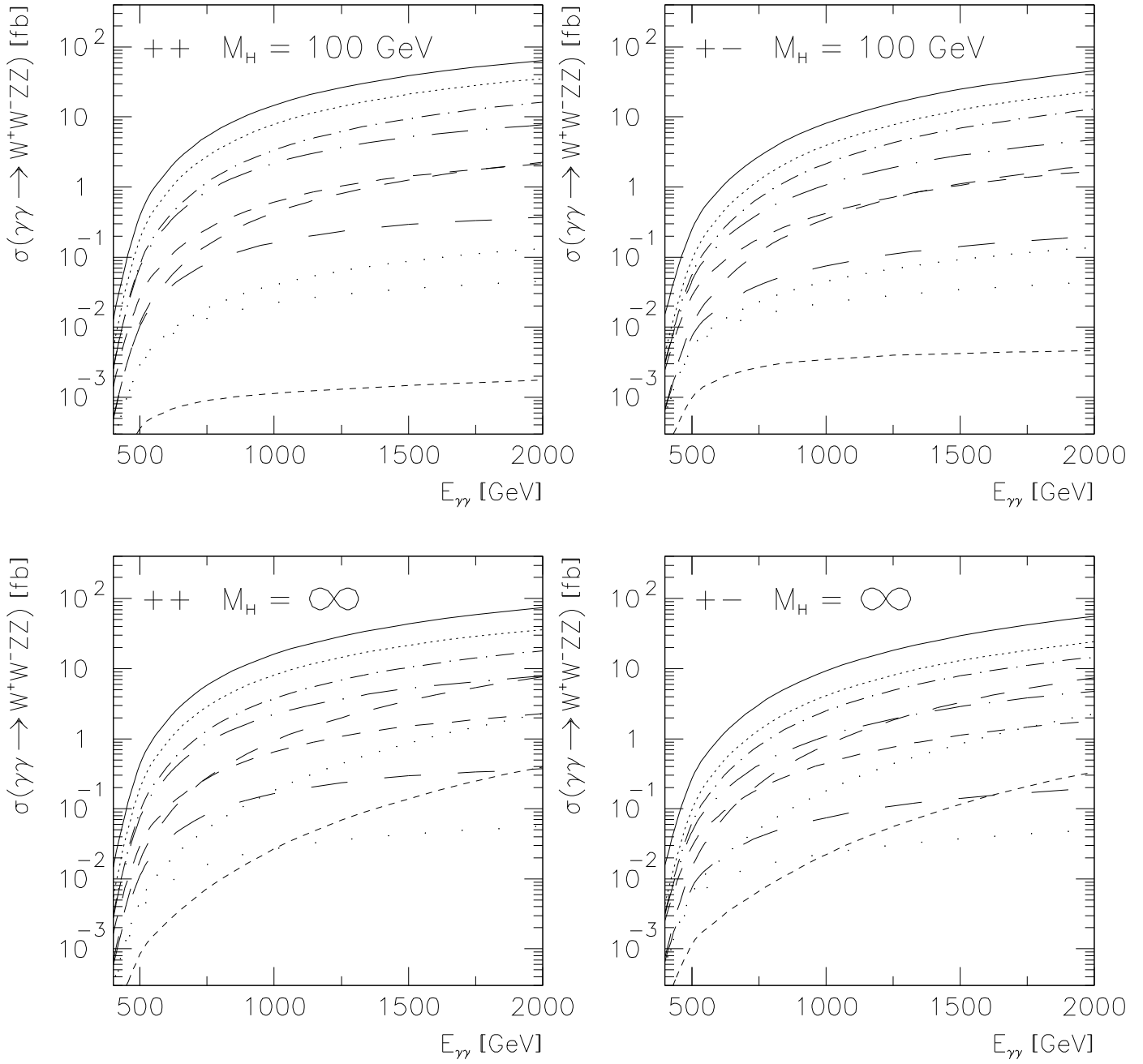


Figure 6.

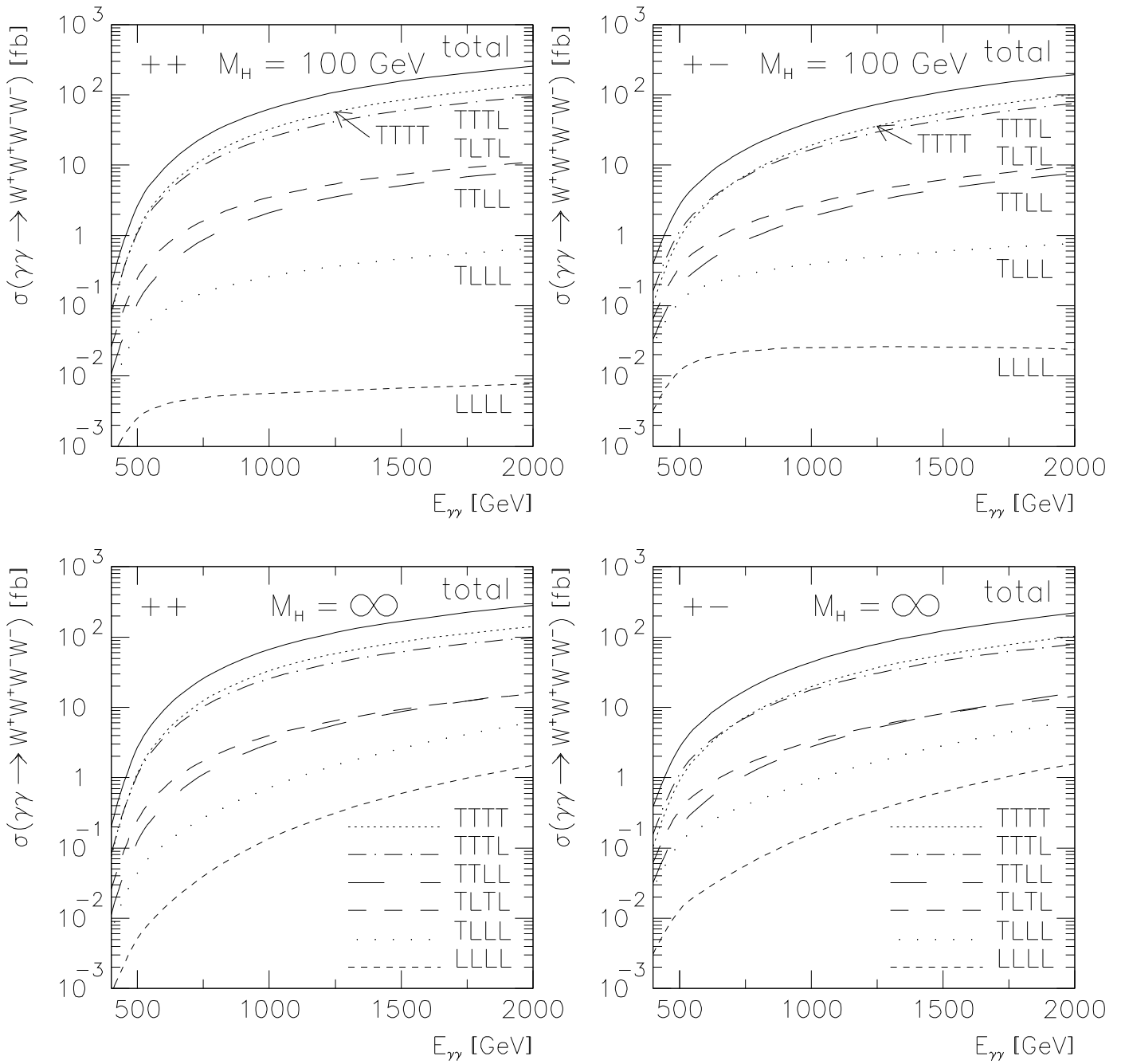


Figure 7.

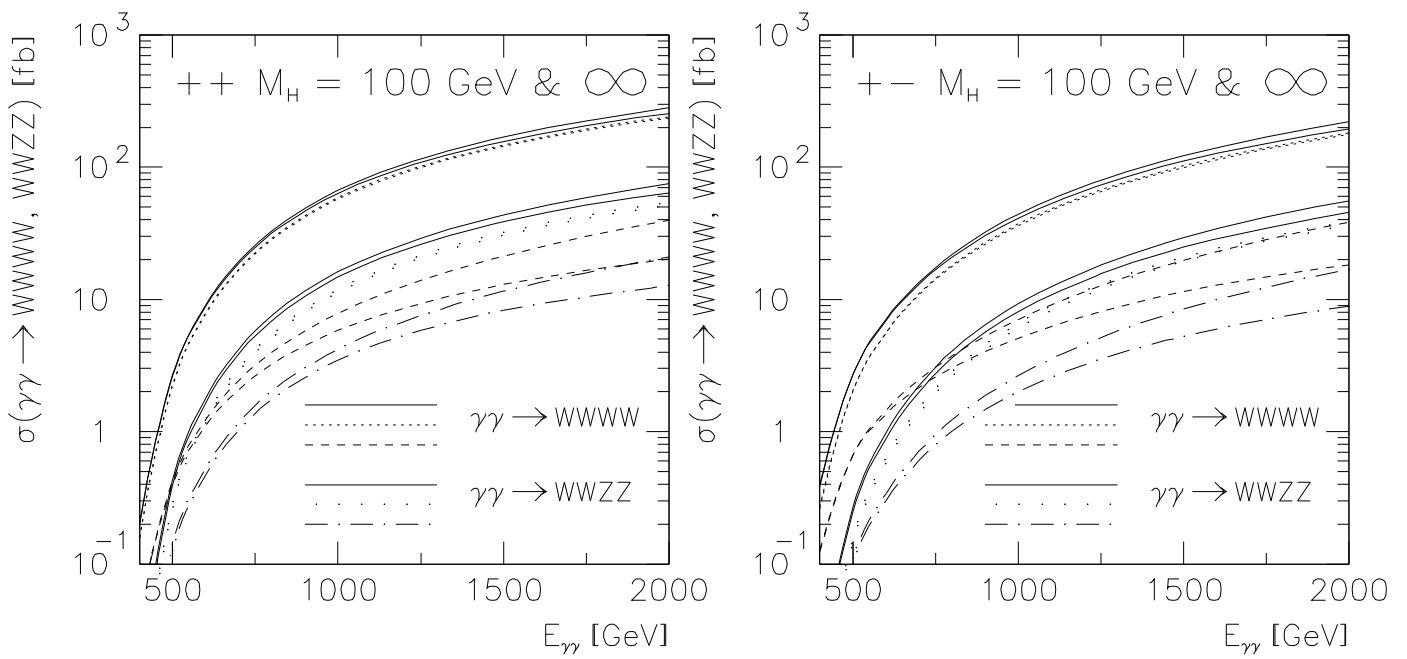


Figure 8.

$\sqrt{s} = 2000 \text{ GeV}$ ,  $M_H = 100 \text{ GeV}$  &  $1000 \text{ GeV}$

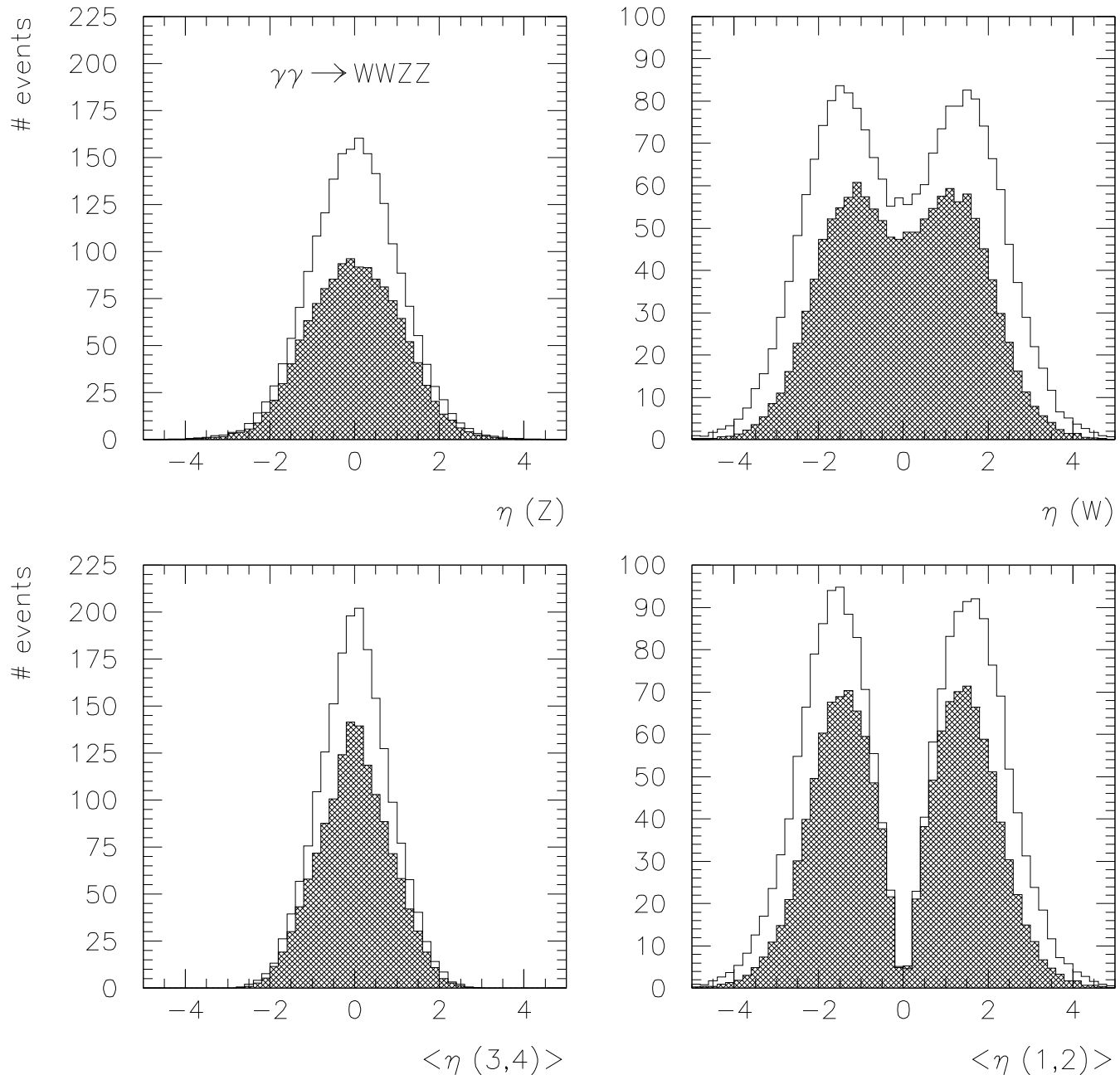


Figure 9.

$\sqrt{s} = 2000 \text{ GeV}$ ,  $M_H = 100 \text{ GeV}$  &  $1000 \text{ GeV}$

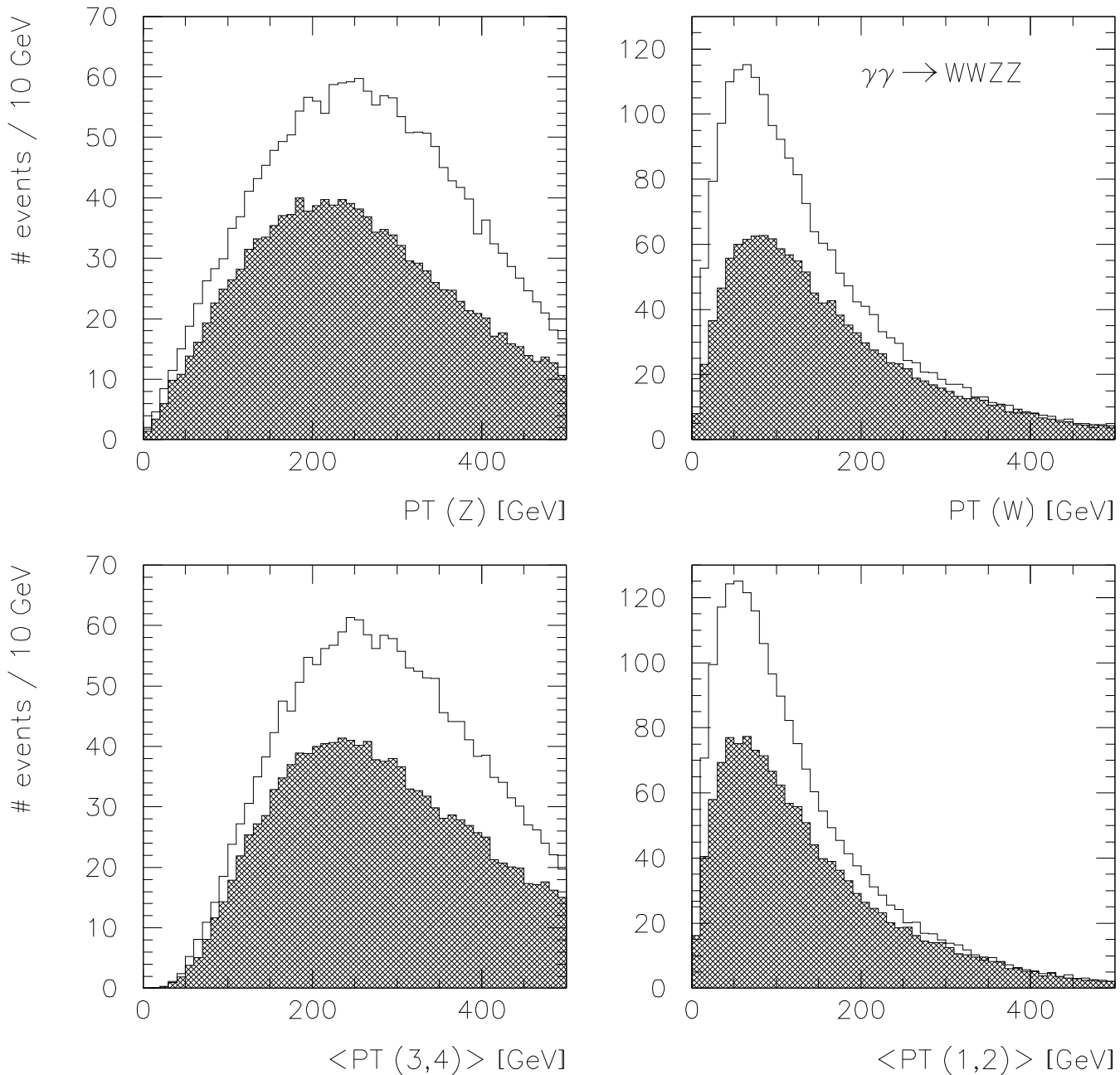


Figure 10.

$\sqrt{s} = 2000 \text{ GeV}$ ,  $M_h = 100 \text{ GeV}$  &  $1000 \text{ GeV}$

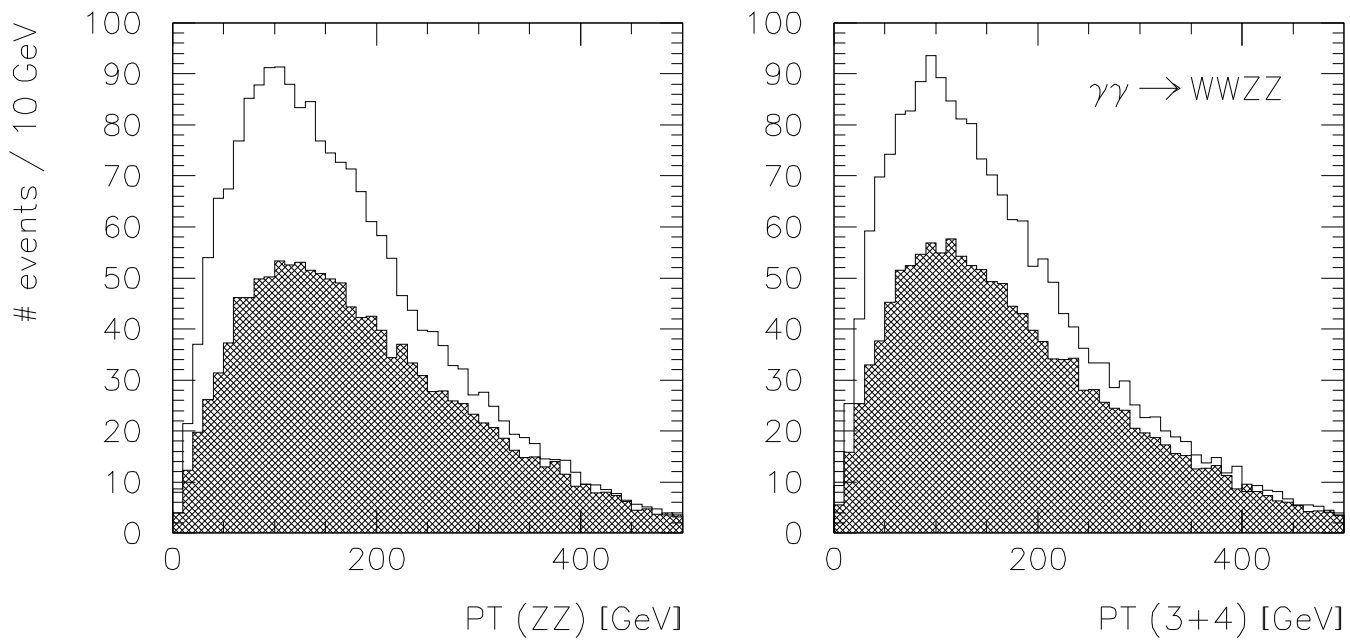


Figure 11.

$\sqrt{s} = 2000 \text{ GeV}$ ,  $M_H = 100 \text{ GeV}$  &  $1000 \text{ GeV}$

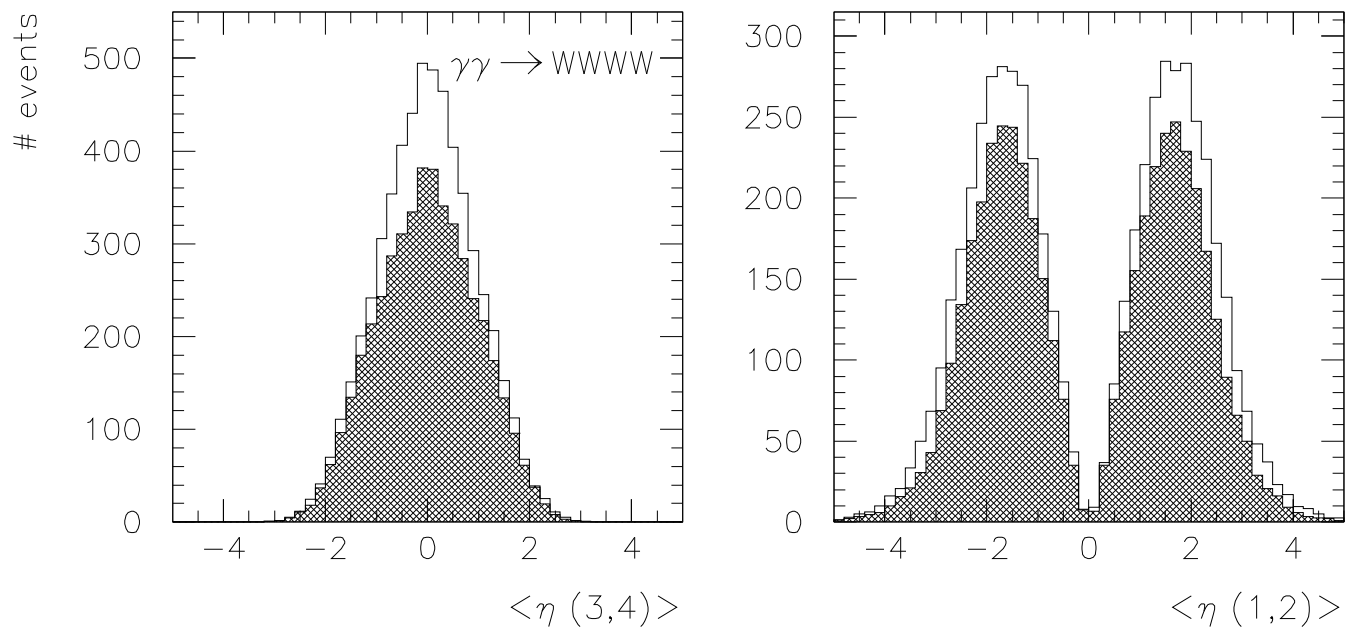


Figure 12.

$\sqrt{s} = 2000 \text{ GeV}$ ,  $M_H = 100 \text{ GeV}$  &  $1000 \text{ GeV}$

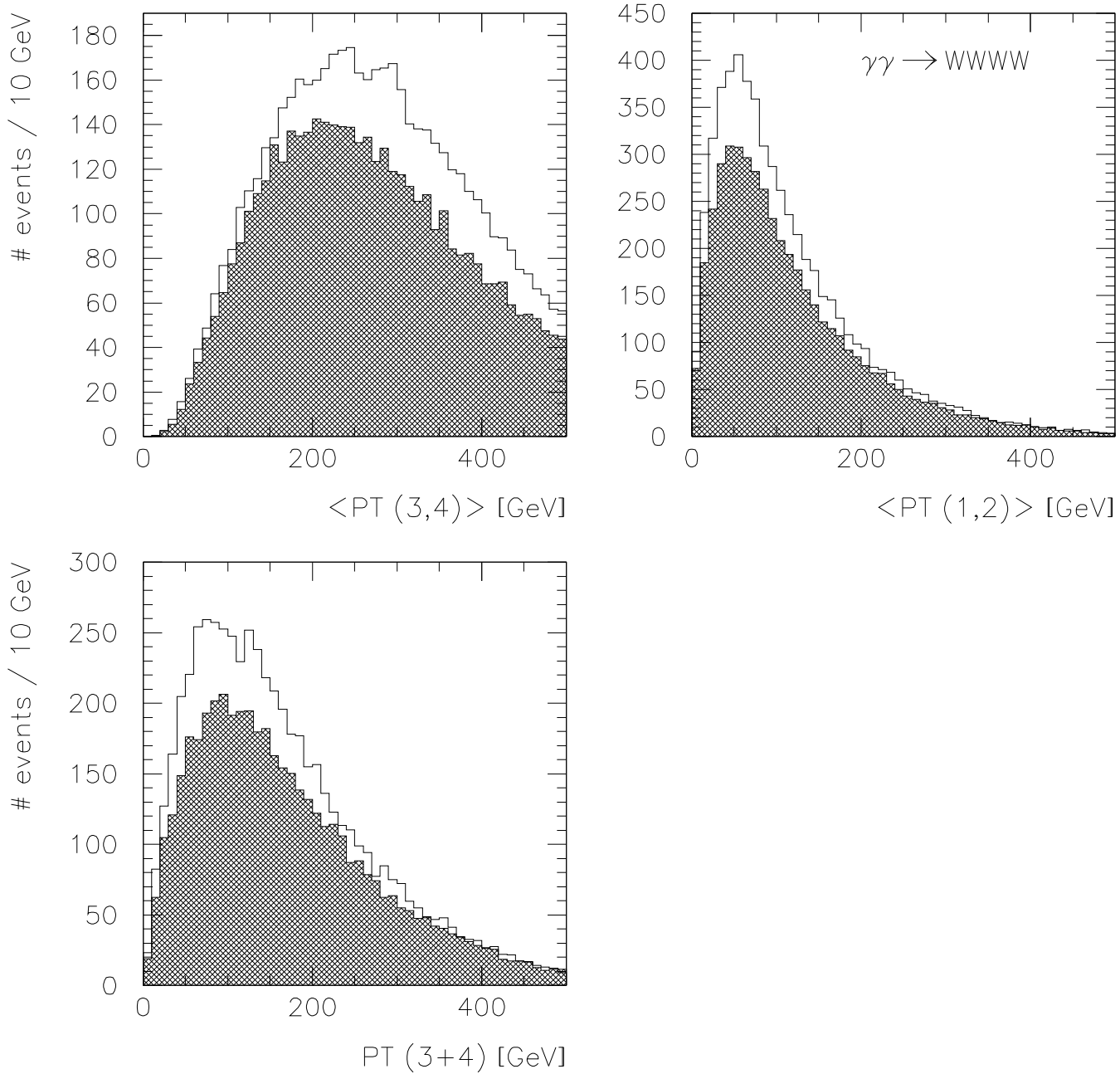


Figure 13.

$\sqrt{s} = 2000 \text{ GeV}$ ,  $M_H = 100 \text{ GeV}$  &  $1000 \text{ GeV}$

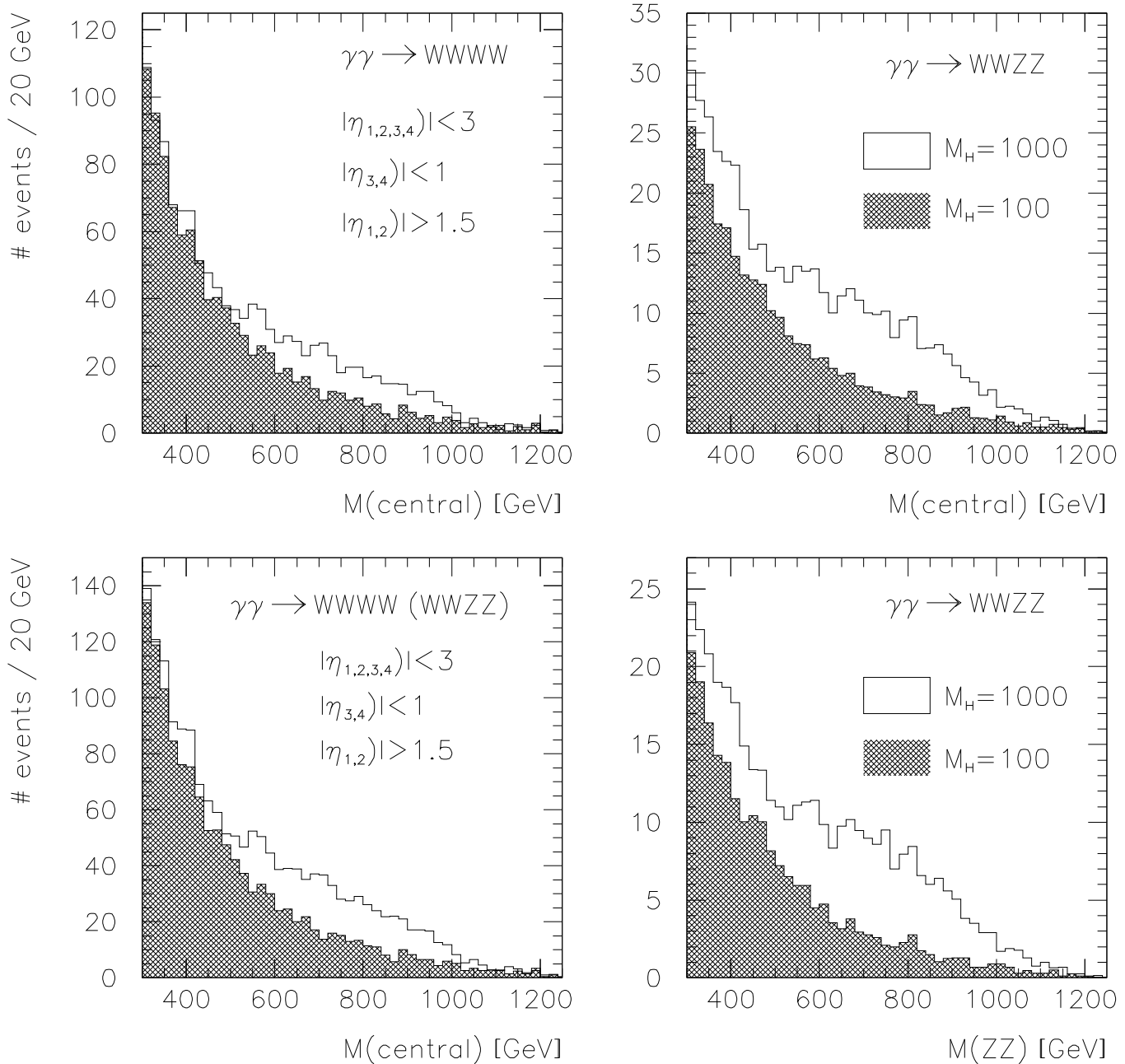


Figure 14.

$\sqrt{s} = 1500 \text{ GeV}, M_H = 100, 500 \text{ & } 700 \text{ GeV}$

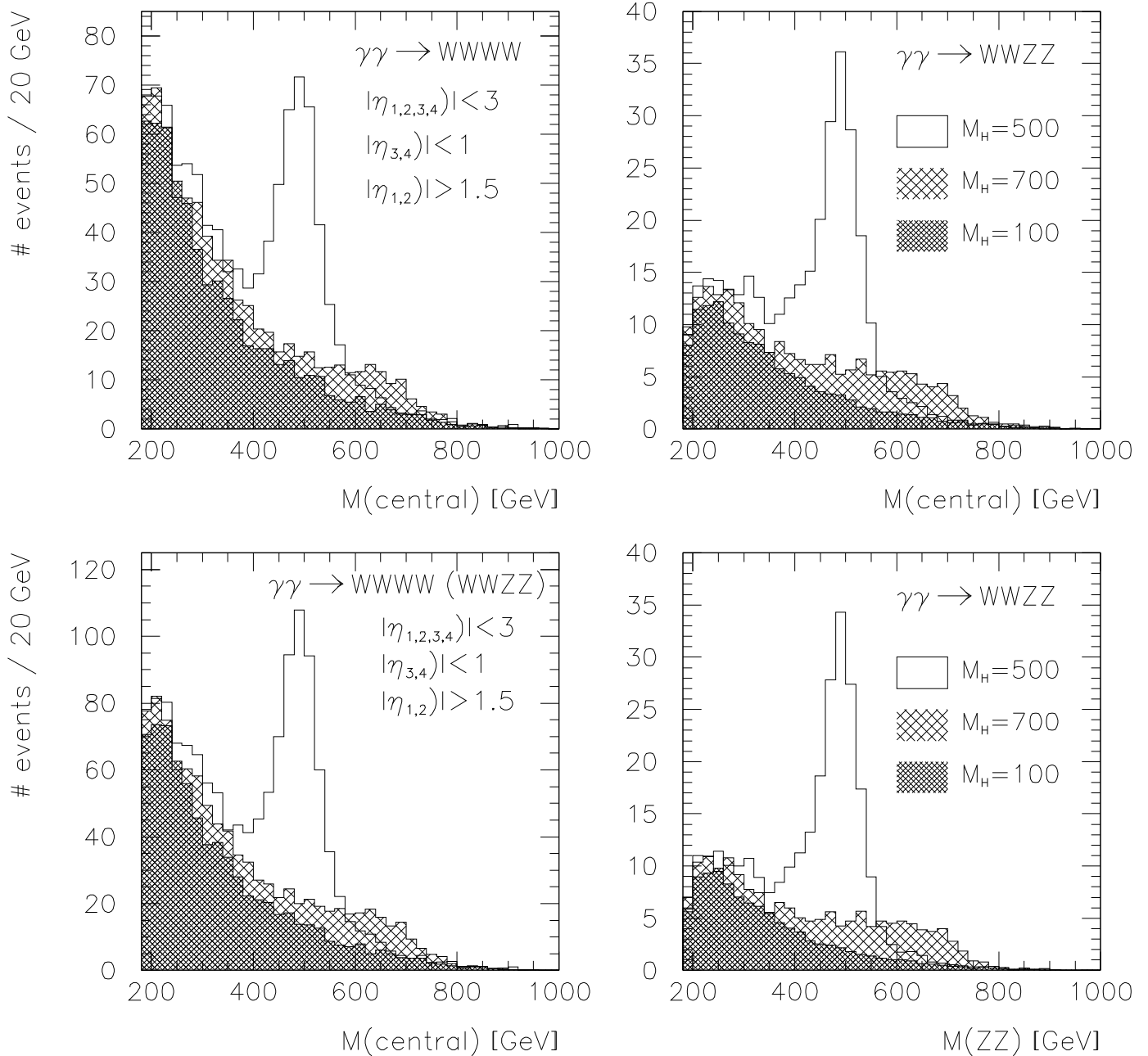


Figure 15.

$\sqrt{s} = 3000 \text{ GeV}$ ,  $M_H = 100 \text{ GeV}$  &  $\infty$

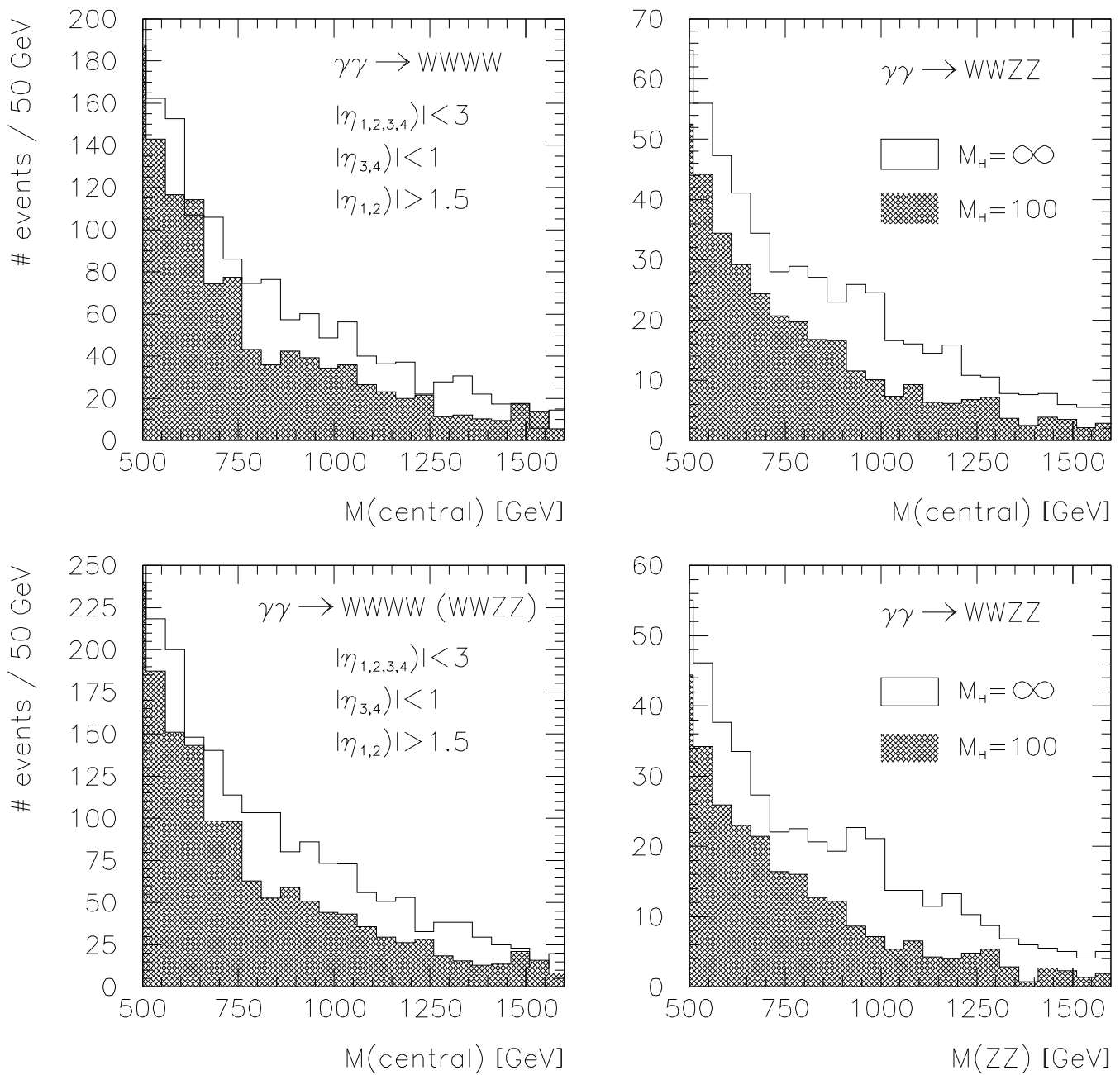


Figure 16.

This figure "fig1-1.png" is available in "png" format from:

<http://arxiv.org/ps/hep-ph/9407393v1>

This figure "fig1-2.png" is available in "png" format from:

<http://arxiv.org/ps/hep-ph/9407393v1>

This figure "fig1-3.png" is available in "png" format from:

<http://arxiv.org/ps/hep-ph/9407393v1>

This figure "fig1-4.png" is available in "png" format from:

<http://arxiv.org/ps/hep-ph/9407393v1>

This figure "fig1-5.png" is available in "png" format from:

<http://arxiv.org/ps/hep-ph/9407393v1>

This figure "fig1-6.png" is available in "png" format from:

<http://arxiv.org/ps/hep-ph/9407393v1>

This figure "fig1-7.png" is available in "png" format from:

<http://arxiv.org/ps/hep-ph/9407393v1>

This figure "fig1-8.png" is available in "png" format from:

<http://arxiv.org/ps/hep-ph/9407393v1>

This figure "fig1-9.png" is available in "png" format from:

<http://arxiv.org/ps/hep-ph/9407393v1>

This figure "fig1-10.png" is available in "png" format from:

<http://arxiv.org/ps/hep-ph/9407393v1>

This figure "fig1-11.png" is available in "png" format from:

<http://arxiv.org/ps/hep-ph/9407393v1>

This figure "fig1-12.png" is available in "png" format from:

<http://arxiv.org/ps/hep-ph/9407393v1>

This figure "fig1-13.png" is available in "png" format from:

<http://arxiv.org/ps/hep-ph/9407393v1>

This figure "fig1-14.png" is available in "png" format from:

<http://arxiv.org/ps/hep-ph/9407393v1>

This figure "fig1-15.png" is available in "png" format from:

<http://arxiv.org/ps/hep-ph/9407393v1>

This figure "fig1-16.png" is available in "png" format from:

<http://arxiv.org/ps/hep-ph/9407393v1>